ABSTRACT

Title of Dissertation: TRAJECTORY OPTIMIZATION OF A TETHERED UNDERWATER KITE

Miguel Alvarez Tiburcio
Doctor of Philosophy, 2021

Dissertation Directed by: Professor Hosam Fathy
Department of Mechanical Engineering

This dissertation addresses the challenge of optimizing the motion trajectory of a tethered marine hydrokinetic energy harvesting kite in order to maximize its average electric power output. The dissertation focuses specifically on the "pumping" kite configuration, where the kite is periodically reeled out from a floating base station at high tension, then reeled in at low tension. This work is motivated by the significant potential for sustainable electricity generation from marine currents such as the Gulf Stream. Tethered systems can increase their energy harvesting potential significantly through cross-current motion. Such motion increases apparent flow speed, which is valuable because the instantaneous maximum power that can be harvested is proportional to the cube of this apparent speed. This makes it possible for tethered systems to achieve potentially very attractive power densities and levelized costs of electricity compared to stationary turbines. However, this also necessitates the use of trajectory optimization and active control in order to eke out the maximum energy harvesting capabilities of these systems.

The problem of optimizing the trajectories of these kites is highly non-linear and thus challenging to solve. In this dissertation we make key simplifications to both the modeling and the structure of the optimal solution which allows us to learn valuable insights in the nature of the power maximizing trajectory. We first do this analysis to maximize the average mechanical power of the kite, then we expand it to take into account system losses. Finally, we design and fabricate an experimental setup to both parametrize our model and validate our trajectories.

In summary, the goal of this research is to furnish model-based algorithms for the online optimal flight control of a tethered marine hydrokinetic system. The intellectual merit of this work stems from the degree to which it will tackle the difficulty of solving this co-optimization problem taking into account overall system efficiency and the full range of possible system motion trajectories. From a broader societal perspective, this work represents a step towards experimentally validating the potential of pumped underwater kite systems to serve as renewable energy harvesters in promising environments such as the Gulf Stream.

TRAJECTORY OPTIMIZATION OF A TETHERED UNDERWATER KITE

by

Miguel Alvarez Tiburcio

Dissertation submitted to the Faculty of the Graduate School of the
University of Maryland, College Park in partial fulfillment
of the requirements for the degree of
Doctor of Philosophy
2021

Advisory Committee:
Professor Hosam Fathy, Chair/Advisor
Professor Amr Baz
Professor Nikhil Chopra
Professor Alireza Khaligh, Dean's Representative
Professor Michael Otte
Professor Eleonora Tubaldi

Table of Contents

List of Figures **iv**

Chapter 1:Introduction **1**
1.1 Vision and Motivation 1
1.2 Literature Review 3
1.2.1 Modeling of tethered kite systems 3
1.2.2 Controlling tethered kite systems 6
1.3 Open Challenges and Contributions 7

Chapter 2:Development of a simplified model of the dynamics of a marine hydrokinetic energy harvesting system and its tether **10**
2.1 Chapter introduction 10
2.2 3DOF Kite Model 10
2.3 Tether Model 15
2.4 Model Comparison 19
2.5 Chapter conclusion 22

Chapter 3:Outcomes and Insights from Simplified Analytic Trajectory Optimization for a Tethered Underwater Kite **23**
3.1 Chapter introduction 23
3.2 Kite Model 25
3.3 Problem Formulation 30
3.3.1 Optimization Objective 30
3.3.2 Model Linearization 31
3.3.3 Simplified Optimization Problem 32
3.3.4 Analytical Solution 33
3.4 Results 36
3.4.1 Performance Metric 36
3.4.2 Kite Linear Quadratic Regulator 36
3.4.3 Numerical Simulation 37
3.4.4 Sensitivity to eigenvector scaling 39
3.5 Chapter conclusion 41

Chapter 4: Modeling and Trajectory Generation with Electrical and Mechanical Losses **44**
4.1 Chapter introduction . . . 44
4.2 Modeling of the electric machine . . . 44
4.3 Problem formulation . . . 46
4.4 Simulation & Results . . . 47
4.5 Chapter conclusion . . . 51

Chapter 5: Design & Fabrication of Prototype Power Take-Off System for a Lab Scale MHK **54**
5.1 Chapter introduction . . . 54
5.2 Pool-test PTO . . . 55
5.3 Lake test PTO . . . 57
5.4 Laboratory Experiments . . . 58
5.5 Parameter identification . . . 60
5.6 Chapter conclusion . . . 62

Chapter 6: Summary and Conclusions **65**
6.1 Summary . . . 65
6.2 Future work . . . 66

Bibliography **67**

List of Figures

1.1 Energy consumption from major renewable sources in quad BTU. Source: Department of Energy [1] . . . 1
1.2 Total energy consumption by type [quad BTU]. Source: Department of Energy [1] . . . 2
1.3 Visualization of the Gulf Stream WBC. Source: windy.com . . . 3
1.4 Underwater kite prototype with on-board turbine. Source: Minesto AB [2] . . . 4
1.5 Underwater kite tethered to floating platform . . . 5

2.1 Diagram of 3DOF kite, $w-$frame, and external forces . . . 11
2.2 Elastic tether coordinates . . . 15
2.3 Infinitesimal tether element . . . 16
2.4 Trajectory followed by the kite (in blue). Tether (grey) at different moments in time . . . 20
2.5 Deviations due to increasing mass for a neutrally buoyant tether . . . 20
2.6 Deviations due to buoyancy effects . . . 21

3.1 Underwater kite with unit vectors in Cartesian and spherical coordinates . . . 26
3.2 Water frame and external forces . . . 28
3.3 Path of the non-linear kite model in the last 3 periods of simulation . 39
3.4 Power generated in the last period of simulation.Orange line: Non-linear model, Blue line: Linear model. . . . 40
3.5 Release rate and tension for the last period of simulation. Orange line: Non-linear model, Blue line: Linear model. . . . 41
3.6 Average power generated by non-linear model vs. average power generated by linear model as the scaling factor λ increases . . . 42

4.1 Release rate and tension trajectories by optimizing for mechanical and electrical power — Linearized model . . . 49
4.2 Electric power trajectories by optimizing for mechanical and electrical power . . . 49
4.3 Release rate and tension trajectories optimized for electrical power and tracked by LQR controller. . . . 50
4.4 Kite path in Cartesian coordinates . . . 50

5.1 Description of PTO . . . 55

5.2 3D CAD of PTO prototype 56
5.3 PTO connections diagram 57
5.4 Picture of PTO pulling raft during pool testing 58
5.5 Diagram of PTO for lake test and its sensors. 59
5.6 Picture of PTO for lake test that supports an additional motor on the bottom shaft. 60
5.7 Measured release rate and tension during three periods. 61
5.8 Measured mechanical power and electrical power of PTO during three periods. 62
5.9 Generated mechanical and electrical energy during three periods. . . . 63
5.10 Measured power loss and predicted loss using estimated parameters . 64
5.11 Measured mechanical power, measured electrical power, and electrical power prediction w/ estimated parameters 64

Chapter 1: Introduction

1.1 Vision and Motivation

This dissertation examines the problem of optimizing the periodic flight trajectory of a tethered marine hydrokinetic (MHK) kite in order to maximize the average electric power it is able to harvest. Broadly speaking, therefore, this work represents a contribution to the domain of the optimal control of renewable energy harvesting systems. Renewable energy sources like solar and wind have made significant gains in generation, increasing by 190% and 57% respectively from 2015 to 2020 in the United States [1] shown in Figure 1.1. While this progress is significant, it is still far from reducing our dependency on fossil fuels, as shown in Figure 1.2.

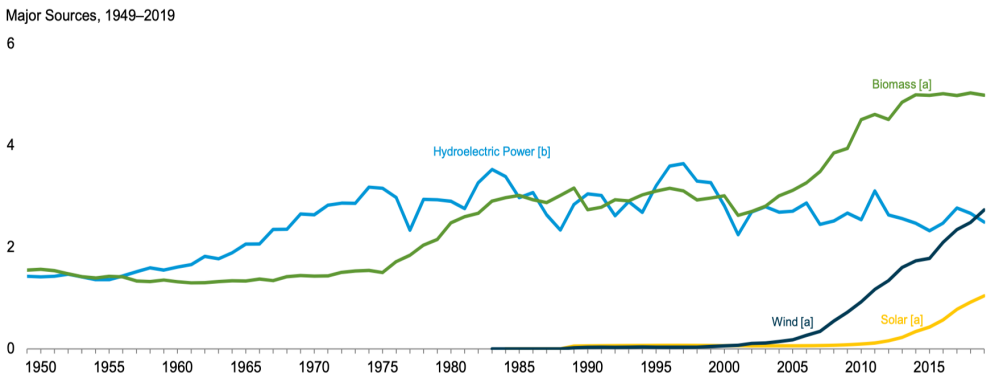

Figure 1.1: Energy consumption from major renewable sources in quad BTU. Source: Department of Energy [1]

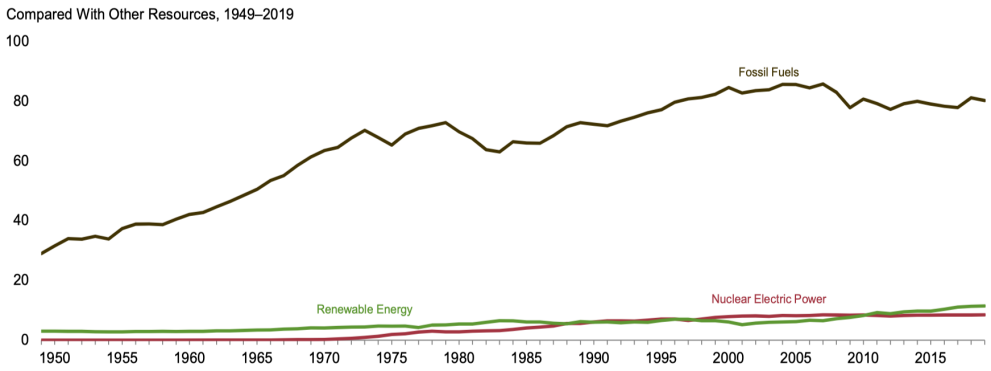

Figure 1.2: Total energy consumption by type [quad BTU]. Source: Department of Energy [1]

One potential source of energy that remains relatively unexploited is that of the ocean currents. This includes western boundary currents (WBC), which flow in the western regions of oceans along continental shores. These WBCs have a typical width of 100 km and height of 1000 m with speeds that can reach $3\,\mathrm{m\,s^{-1}}$ [3]. One example of these currents is the Gulf Stream that flows along the continental United States as can be seen in Figure 1.3. For instance, measurements near the North Carolina shore at a depth of 75 m yielded a mean current speed of $1.07\,\mathrm{m\,s^{-1}}$ for an entire year of measurements [3]. We can estimate the power density of the water as:

$$P = \frac{1}{2}\rho v^3 \tag{1.1}$$

where, P, ρ and v are the power density in $\mathrm{W\,m^{-2}}$, the density of water, and the speed of the fluid respectively. This suggests that the Gulf Stream at that location has an average power density of $1000\,\mathrm{W\,m^{-2}}$.

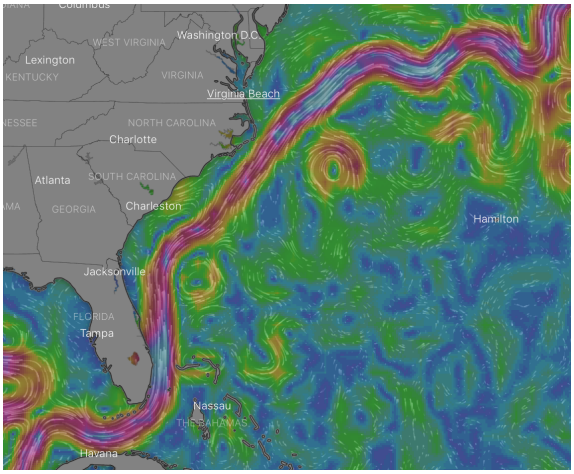

Figure 1.3: Visualization of the Gulf Stream WBC. Source: windy.com

1.2 Literature Review

Multiple types of marine hydrokinetic systems have been proposed to extract energy from the above currents, including marine hydrokinetic kites. The evolution of these kites was initially inspired by tethered airborne wind energy systems (AWES) [4], largely motivated by seminal research by Loyd in 1980 [5]. Both of these types of systems rely on flying cross-current to amplify the apparent kite speed relative to the surrounding fluid. They generate electricity either with an on-board generator (e.g., Figure 1.4), or by reeling out a tether attached to a generator in a stationary platform as shown in Figure 1.5. The latter "pumping" configuration is the focus of this work.

1.2.1 Modeling of tethered kite systems

The problem of maximizing the energy tethered underwater kites harvest is challenging because it involves the optimization of a trajectory in a large configura-

Figure 1.4: Underwater kite prototype with on-board turbine. Source: Minesto AB [2]

tion space. This motivates the need for simple models, amenable to optimization, that capture the relevant dynamics of the system. In general there is a trade-off between model accuracy and model simplicity. A simplified control-oriented model is more useful to design a controller, while a more accurate model is more useful for evaluating the controller performance.

Control-oriented models of energy-harvesting kites do not typically include the tether dynamics, but only focus on modeling the dynamics of the given kite with different levels of complexity. For instance, in the AWES literature, some models assume the kite is massless and produce a static relationship that is useful for approximating the power generated by the system when moving at a constant speed [5–8]. While this assumption is very useful for the design of simple controllers for lightweight flexible AWES, neglecting the kite dynamics is not valid for the

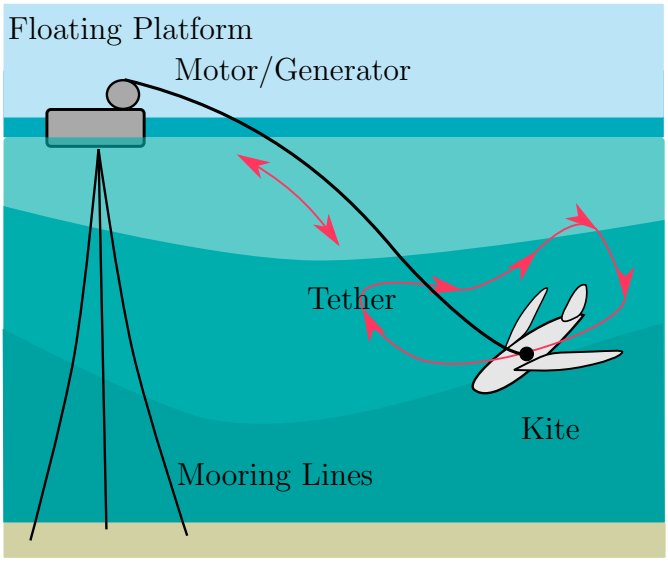

Figure 1.5: Underwater kite tethered to floating platform

heavier rigid-wing kites. To address that fact, other work treats the kite as a point mass, which makes it possible to include the translational kite dynamics in their model. This can be done in 2 dimensions, like the sailboat model used in [9], or in 3 dimensions [10–14]. Treating the kite as a point mass neglects its rotational dynamics. That is why higher-order—airplane-like—kite models are also used in the literature. These kite models are inspired by the typical 6DOF airplane flight dynamic models [4, 15–20].

Higher-order models include 6DOF kite models and a tether model. One way the tether is modeled is by treating it as a chain of discrete lumped masses. These can be connected elastically (with spring-dampers) or inelastically [12, 20–23]. An alternative, more accurate way of modeling the tether is to use partial differential equations to describe the dynamics of every infinitesimal element along the tether. This approach is not common in either the AWES or marine hydrokinetic literature, but has been explored in other contexts, for example: (i) the study of instrumented

marine cables in surveying boats [24] and, (ii) the study of tethers of underwater remotely operated vehicles [23].

1.2.2 Controlling tethered kite systems

Tethered kite systems rely on being actively controlled to generate energy. Typically, the kite trajectory will consist of a high tension regime as the kite is reeled out, and a low tension regime as the kite is reeled in. Given the importance of control in the energy generation potential of MHK systems, significant research focuses on the design of these controllers.

The first challenge the literature addresses is the trajectory optimization of these systems. Naturally the overall objective is maximizing the net power generation of the system. Because of the complexity of the optimization problem, this is typically done by separating the problem into a power generating phase, and a power consuming phase. Moreover, the objective is simplified by maximizing a proxy to the generated power, such as tension force [25, 26]. Other work in the AWES literature simplifies the optimization problem by pre-imposing a topological constraint to the kite path, forcing it to navigate in figure-8 shapes. Optimization then proceeds using direct transcription [27, 28].

The other challenge the literature addresses is how the kite trajectory adapts to the changing nature of wind currents (for AWES) or ocean currents (for MHK). That is why a big part of the literature focuses on developing adaptive controllers. This includes: robust and passivity-based control [7, 17], extremum-seeking [11],

Bayesian optimization [9, 29], iterative learning [30, 31], and maximum power point tracking [32].

1.3 Open Challenges and Contributions

From the literature reviewed in the previous section, we have identified a set of open challenges that we propose to address:

1. First, it is not clear from the literature whether an integrated model of the dynamics of a marine hydrokinetic kite system plus its flexible tether is needed for optimal control. There is work in the literature on kite modeling, tether modeling, and the integrated modeling of kite systems plus their tethers. However, there is a shortage of studies examining the interplay between kite and tether dynamics and elucidating the degree to which this interplay affects overall system behavior. The research addresses this problem by developing a 3-DOF kite model plus a partial differential equation (PDE) tether model. Integrating these models together makes it possible to examine the above interplay, and determine its impact on overall system behavior, for different values of the tether parameters. One conclusion from this study is that the importance of incorporating tether dynamics in the overall kite system model depends critically on factors such as the tether material's buoyancy.

2. Second, the existing literature on trajectory optimization for tethered marine hydrokinetic systems suffers from multiple deficiencies. Moreover, the literature typically simplifies the kite trajectory optimization problem by ei-

ther pre-imposing a specific flight path and optimizing its parameters or optimizing the reel-in/reel-out and cross-current motions independently. Such a divide-and-conquer approach, while appealing from a numerical perspective, has the potential to lead to sub-optimal trajectories. The proposed research addresses these deficiencies by formulating a co-optimization problem that attempts to optimize both the reel-in/reel-out and cross-current motion trajectories simultaneously. The above co-optimization problem is computationally challenging because it involves trajectory optimization over a large configuration space. Given this computational complexity, we use a 3DOF model of the kite in spherical coordinates and linearize it around a zero-power circular cross-current equilibrium trajectory. This makes it possible to formulate power maximization as a simple indefinite quadratic optimal control problem with linear dynamic constraints. By imposing sinusoidal inputs it is possible to analytically obtain trajectories that generate power with a good Loyd factor.

3. Third, in the literature, trajectory optimization for these systems often attempts to maximize the average mechanical power output over one reel-in/reel-out period, without accounting for electrical conversion efficiency. In chapter 4 using the techniques developed in chapter 3 we modify our model to take into account these losses and re-optimize our trajectories.

4. Fourth, there is a growing need for laboratory-scale studies validating trajectory optimization solutions for tethered marine hydrokinetic energy harvesters. In chapter 5 we design and and fabricate a prototype power takeoff system

capable of demonstrating the reel-in behavior of the kite. Experimental pool tests were performed in close collaboration with North Carolina State University. Additionally, we design and fabricate another prototype capable of both reel-in and reel-out in preparation for tests in Lake Norman, North Carolina. In the laboratory this setup is used to evaluate the potential of our optimized trajectories to generate electrical power, and identify the parameters of the electrical system.

Chapter 2: Development of a simplified model of the dynamics of a marine hydrokinetic energy harvesting system and its tether

2.1 Chapter introduction

This chapter begins by modeling a simplified 3DOF kite that assumes a straight, mass-less tether. Then we derive a flexible tether model using partial differential equations. At the end of the chapter we explore the importance of modeling the curvature and inertia of the kite tether. This work was published and presented at the Proceedings of the 2021 European Control Conference (ECC).

2.2 3DOF Kite Model

We need a simplified model of the system that is amenable to optimization. We propose to model a neutrally buoyant kite with three degrees of freedom (3DOF) constrained by a straight mass-less tether. We make the following assumptions:

1. The desired kite attitude trajectory (i.e., roll, pitch, and yaw angles vs. time) can be tracked through a lower-level control system, thereby allowing this modeling effort to focus on translational kite dynamics.

2. The kite is neutrally buoyant, so its weight is cancelled by the buoyancy force.

3. The kite weather-cocks, so we can neglect side forces.

The forces that act on the kite are: the tether tension, the hydrodynamic lift, and the hydrodynamic drag. These forces are shown in Figure 2.1. The tether force is externally imposed by a tether model that can represent either a rigid or elastic tether. If the tether is assumed rigid, then the tether force is assumed to be aligned with the unit vector from the kite mass to the tether release point. Moreover, a kinematic constraint on the tether's length makes it possible to compute the tether force. In contrast, if the tether is assumed to be elastic, then the tether force is dictated by the corresponding tether dynamics.

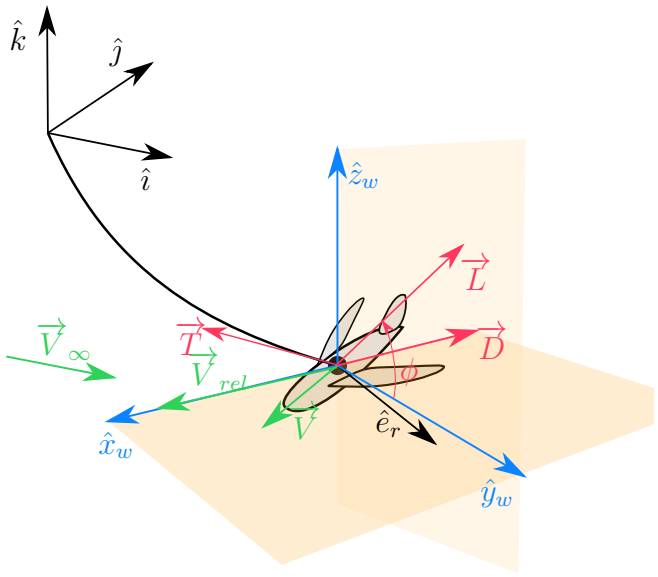

Figure 2.1: Diagram of 3DOF kite, $w-$frame, and external forces

We define the position and velocity of the kite with the respect to the inertial

frame defined by the unit vectors $\left\{\hat{\imath}, \hat{\jmath}, \hat{k}\right\}$

$$\vec{r} = x\hat{\imath} + y\hat{\jmath} + z\hat{k} \tag{2.1}$$

$$\vec{V} = \dot{x}\hat{\imath} + \dot{y}\hat{\jmath} + \dot{z}\hat{k}. \tag{2.2}$$

We further define the position unit vector

$$\hat{e}_r = \frac{\vec{r}}{\|\vec{r}\|} \tag{2.3}$$

and define the relative velocity vector as

$$\vec{V}_{rel} = \vec{V} - \vec{V}_\infty \tag{2.4}$$

where $\vec{V}_\infty$ is the water current velocity. We now define the so-called "wind frame", or w-frame, with the unit vectors $\{\hat{x}_w, \hat{y}_w, \hat{z}_w\}$ defined as

$$\hat{x}_w = \frac{\vec{V}_{rel}}{\|\vec{V}_{rel}\|} \tag{2.5}$$

$$\hat{z}_w = \frac{\hat{x}_w \times \hat{e}_r}{\|\hat{x}_w \times \hat{e}_r\|} \tag{2.6}$$

$$\hat{y}_w = \frac{\hat{z}_w \times \hat{x}_w}{\|\hat{z}_w \times \hat{x}_w\|} \tag{2.7}$$

We can now define the lift and drag forces the kite experiences

$$\vec{L} = \frac{1}{2}\rho C_L(\alpha) S \|\vec{V}_{rel}\|^2 (\cos\phi \hat{y}_w + \sin\phi \hat{z}_w) \tag{2.8}$$

$$\vec{D} = -\frac{1}{2}\rho C_D(\alpha) S \|\vec{V}_{rel}\|^2 \hat{x}_w \tag{2.9}$$

where $\rho, C_L, C_D, \alpha, S,$ and ϕ are respectively, the water density, the lift coefficient, the drag coefficient, the angle of attack, the wing surface area, and the kite angle with respect to the $\hat{y}_w$ unit vector.

The hydrodynamic coefficients C_L and C_D depend on the kite's angle of attack, α. We use curve fitting to approximate this dependency for angles of attack below the stall point of a particular kite of interest. As shown below, we use a linear approximation for the lift coefficient and a quadratic approximation for the drag coefficient.

$$C_L(\alpha) = c_1\alpha + c_2 \tag{2.10}$$

$$C_D(\alpha) = b_1\alpha^2 + b_2\alpha + b_3 \tag{2.11}$$

The sum of external forces is

$$\vec{F}_{ext} = \vec{L} + \vec{D} + \vec{T} \tag{2.12}$$

where $\vec{T}$ is the tether tension force. If the tether is assumed to be rigid, this force

points to the tether platform, in the opposite direction to the $\hat{e}_r$ unit vector:

$$\vec{T} = -T\hat{e}_r \tag{2.13}$$

We can now write a state-space model for the kite

$$\frac{d}{dt}\begin{bmatrix} x \\ y \\ z \\ u \\ v \\ w \end{bmatrix} = \begin{bmatrix} u \\ v \\ w \\ \frac{1}{m}\vec{F}_{ext} \cdot \hat{i} \\ \frac{1}{m}\vec{F}_{ext} \cdot \hat{j} \\ \frac{1}{m}\vec{F}_{ext} \cdot \hat{k} \end{bmatrix} \tag{2.14}$$

where the inputs are:

$$U = \begin{bmatrix} T \\ \alpha \\ \phi \end{bmatrix} \tag{2.15}$$

The mechanical power P_{mech} this kite generates is the product of the tension force T and the tether release rate u_r, where we calculate u_r as follows:

$$u_r = \frac{ux + vy + wz}{\sqrt{(x^2 + y^2 + z^2)}} \tag{2.16}$$

2.3 Tether Model

While the assumption of the tether being straight is useful in the context of optimal control, we do not know the effect of modeling a flexible tether on the kite dynamics. That is in fact the question we were set to answer in [33]. We model the tether dynamics with a system of partial differential equations that capture both the effect of tether buoyancy on the tether and its inertial properties. In this section we describe this tether model and then discuss the conclusions of that paper.

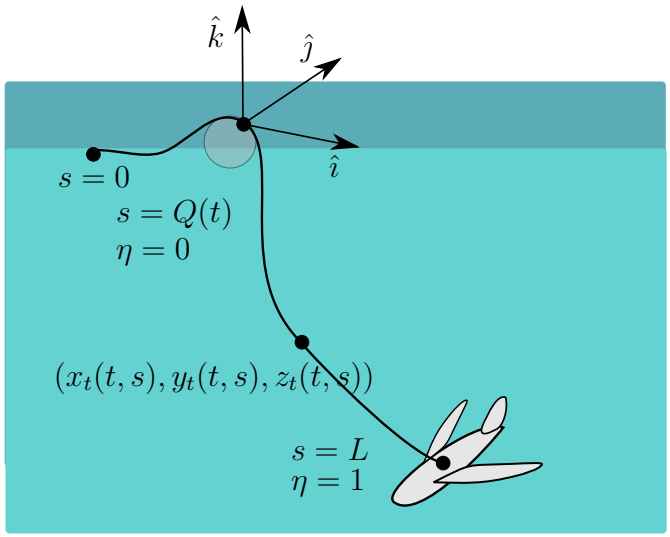

Figure 2.2: Elastic tether coordinates

We define the following coordinates for the tether:

1. s: Distance along undeflected tether.

2. η: Normalized coordinate along undeflected tether.

3. L: Total tether length.

4. $Q(t)$: Unreleased tether length.

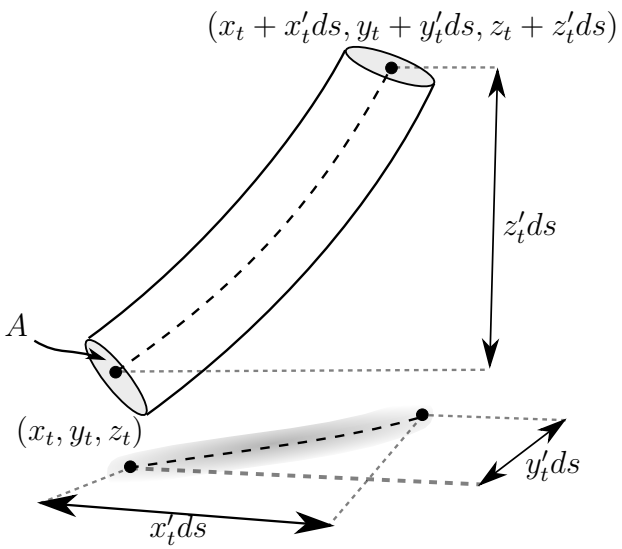

Figure 2.3: Infinitesimal tether element

We also define the absolute position of a point in the tether with respect to the inertial frame $\{\hat{\imath}, \hat{\jmath}, \hat{k}\}$ as: $\{x_t(t,s), y_t(t,s), z_t(t,s)\}$.

Now let us consider the infinitesimal element of the tether in Figure 2.3. We define ds as an infinitesimal change along the $s-$coordinate, and define $x'_t = \frac{\partial x_t}{\partial s}, y'_t = \frac{\partial y_t}{\partial s}, z'_t = \frac{\partial z_t}{\partial s}$.

The strain the element experiences is thus

$$\varepsilon = \frac{\sqrt{x_t'^2 + y_t'^2 + z_t'^2}ds - ds}{ds} \tag{2.17}$$

which simplifies to

$$\varepsilon = \sqrt{x_t'^2 + y_t'^2 + z_t'^2} - 1. \tag{2.18}$$

In the linear deformation region the stress the element experiences is

$$\sigma = E\varepsilon = E(\sqrt{x_t'^2 + y_t'^2 + z_t'^2} - 1) \tag{2.19}$$

where E is Young's modulus of elasticity. Given a cross-sectional area A, the tension this element experiences is

$$T = \sigma A = EA(\sqrt{x_t'^2 + y_t'^2 + z_t'^2} - 1) \tag{2.20}$$

This tension acts along the tether element, with components

$$T_x = T\xi_x \tag{2.21}$$

$$T_y = T\xi_y \tag{2.22}$$

$$T_z = T\xi_z \tag{2.23}$$

where the directional cosines are:

$$\xi_x = \frac{x_t'}{\sqrt{x_t'^2 + y_t'^2 + z_t'^2}} \tag{2.24}$$

$$\xi_y = \frac{y_t'}{\sqrt{x_t'^2 + y_t'^2 + z_t'^2}} \tag{2.25}$$

$$\xi_z = \frac{z_t'}{\sqrt{x_t'^2 + y_t'^2 + z_t'^2}} \tag{2.26}$$

Summing forces and applying Newton's second law to a tether element we obtain the following system of partial differential equations which describe the tether dynamics.

$$\ddot{x}_t = \frac{E}{\rho_t}\frac{\partial}{\partial s}\varepsilon\xi_x + \frac{q_x}{\rho_t} \tag{2.27}$$

$$\ddot{y}_t = \frac{E}{\rho_t}\frac{\partial}{\partial s}\varepsilon\xi_y + \frac{q_y}{\rho_t} \tag{2.28}$$

$$\ddot{z}_t = \frac{E}{\rho_t}\frac{\partial}{\partial s}\varepsilon\xi_z + \frac{q_z}{\rho_t} \tag{2.29}$$

where ρ_t is the density of the tether, and q_{x_t,y_t,z_t} denote additional external forces per unit volume to capture, for example, tether buoyancy effects, gravitational effects, and hydrodynamic effects.

To handle the changing released tether length, we can perform a coordinate transformation to the η-coordinate

$$\ddot{x}_t = \frac{E}{\rho_t(L-Q)}\frac{\partial}{\partial \eta}(\varepsilon\xi_x) + \frac{q_x}{\rho_t} \tag{2.30}$$

$$\ddot{y}_t = \frac{E}{\rho_t(L-Q)}\frac{\partial}{\partial \eta}(\varepsilon\xi_y) + \frac{q_y}{\rho_t} \tag{2.31}$$

$$\ddot{z}_t = \frac{E}{\rho_t(L-Q)}\frac{\partial}{\partial \eta}(\varepsilon\xi_z) + \frac{q_z}{\rho_t} \tag{2.32}$$

$$\dot{Q} = u(t) \tag{2.33}$$

Equations (2.30)-(2.33) constitute the full set of equations necessary to capture the dynamics of tether.

2.4 Model Comparison

The above work makes it possible to build two different MHK system models: one with a rigid tether and one with a flexible tether. We can compare the two models by imposing a trajectory the kite has to follow. We achieve tracking of this trajectory by solving an inverse dynamics model where the trajectory of the kite is given in spherical coordinates by the following algebraic equations:

$$\psi = a_1 \sin(w_1 t) \tag{2.34}$$

$$\theta = a_1 \sin(w_1 t) \cos(w_1 t) + \theta_0 \tag{2.35}$$

as well as the following differential equation:

$$\dot{r} = a_2 \sin w_2 t \tag{2.36}$$

where ψ and θ are the azimuth and zenith angles of the kite with respect to the floating platform. This figure-8 trajectory, while not a power maximizing trajectory, shares the shape of the typical path tethered energy systems follow.

In Figure 2.4 we show the imposed trajectory the kite follows during the reel-out portion of the cycle.

We can, for instance, explore the effect of the tether mass, which we decouple from buoyancy effects by varying the radius of the tether. Figures 2.5a and 2.5b

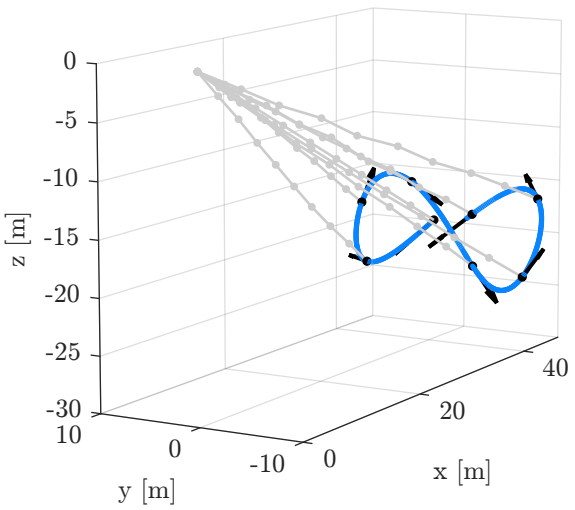

Figure 2.4: Trajectory followed by the kite (in blue). Tether (grey) at different moments in time

show deviations from the nominal input trajectories for three different radii.

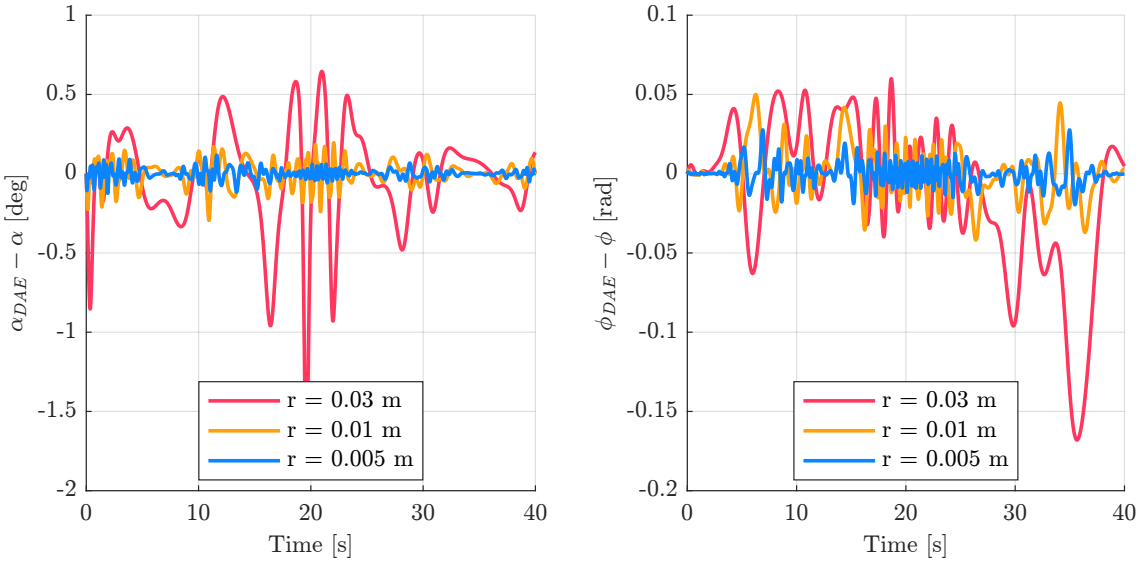

(a) Deviation from nominal angle of attack

(b) Deviation from nominal roll angle

Figure 2.5: Deviations due to increasing mass for a neutrally buoyant tether

We can also explore the effect the buoyancy of the tether has on the kite. In Figures 2.6a and 2.6b we show the deviations from nominal input trajectories for different tether densities. To avoid confounding the buoyancy effect with inertial effects, we ensure the total mass of the tether is maintained constant by adjusting

the radius of the tether as we change the density.

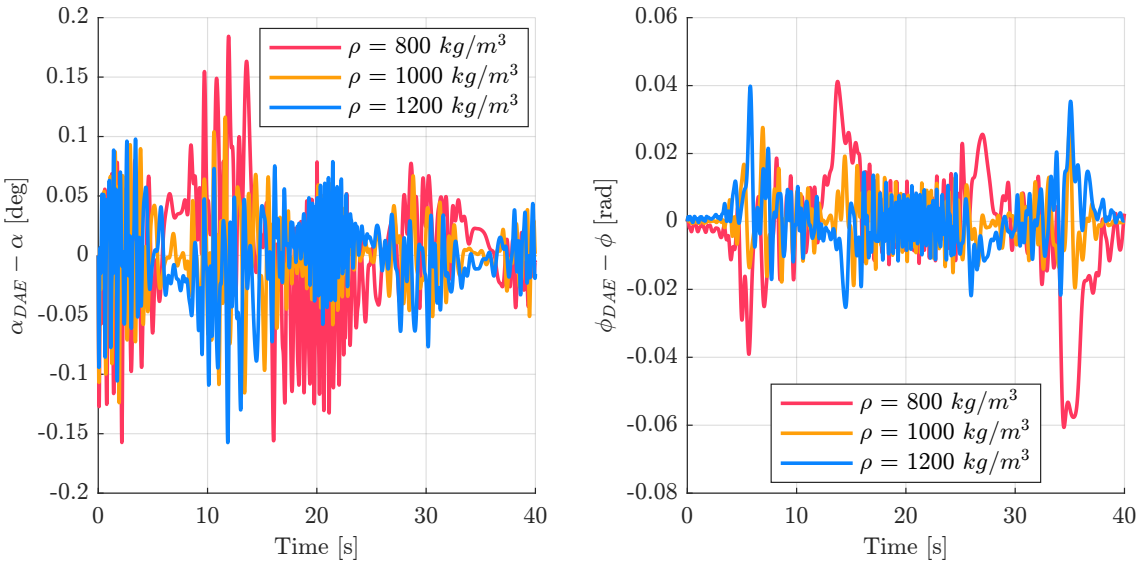

(a) Deviation from nominal angle of attack (b) Deviation from nominal roll angle

Figure 2.6: Deviations due to buoyancy effects

We summarize the results by looking at the root mean squared deviations of these inputs normalized by the root mean squared nominal values, in Table 2.1. Both

	Normalized RMSE in α	Normalized RMSE in ϕ
ρ [kg m^{-3}]		
800	0.0507	0.1601
1000	0.0304	0.067
1200	0.0324	0.0836
r [m]:		
0.005	0.0304	0.0670
0.01	0.0735	0.1586
0.03	0.3207	0.4736
E [Pa]:		
100e9	0.0304	0.0670
200e9	0.0304	0.0670

Table 2.1: Normalized deviations from nominal inputs for different tether parameters

the buoyancy of the tether and the mass of the tether require noticeable corrections of the kite inputs to track the pre-imposed trajectory. On the other hand, the

longitudinal stiffness of the tether had a negligible effect. The effect of buoyancy increases for non-neutrally buoyant tethers. Particularly, the more buoyant tether with a density of $800\,\mathrm{kg\,m^{-3}}$ presents a larger normalized root mean deviation of 16 % from the nominal roll angle trajectory. The effect of mass is however the most significant of the parameters we explore. For instance a 5 mm radius tether has average deviations of 7% from the nominal roll trajectory, while a 3 cm radius tether has average deviations of 47% from the nominal roll trajectory, meaning that it requires considerably more control authority to achieve the desired figure-8 trajectory, than the kite with a mass-less tether. Note that in this work, we vary the tether mass without changing buoyancy by changing the radius of the tether while keeping its density constant.

2.5 Chapter conclusion

At the beginning of this chapter we developed a simplified 3DOF kite model for an underwater kite system. Then we introduced a PDE-based flexible tether model. We explored the effect both the buoyancy of the tether and the inertia of the tether have on the dynamics of the kite. For our specific set of assumptions we conclude it is possible to neglect the tether dynamics for a neutrally buoyant and light tether. A simplified kite model with straight and mass-less tether is used in later chapters.

Chapter 3: Outcomes and Insights from Simplified Analytic Trajectory Optimization for a Tethered Underwater Kite

3.1 Chapter introduction

In this chapter we formulate and solve a periodic trajectory optimization problem for a tethered underwater kite. The goal is to maximize the average mechanical power harvested by the kite. As we explained in the introductory chapter, the problem of optimizing this kite's trajectory is challenging due to the high dimensionality and nonlinearity of its dynamics. To tackle this challenge, the literature often separates the problem into two subproblems focusing on optimizing the cross-current and the reel-in/reel-out components of the trajectory, respectively, which may be sub-optimal. In contrast, this work solves for the combined cross-current and reel-in/reel-out trajectory by linearizing the dynamics of the kite around a zero-power reference equilibrium trajectory in spherical coordinates. This allows the trajectory optimization problem to be solved analytically for simple sinusoidal input perturbations from equilibrium. We use linear quadratic regulation to enable the nonlinear kite model to track the optimized trajectory. The result is a computationally efficient approach that achieves an attractive Loyd factor of 19.9%, while providing

important insights into the nature of the optimal trajectory.

The main goal in this chapter is to simultaneously optimize the reel-in/reel-out and cross-current trajectories of an energy-harvesting kite. The novelty of the contribution in this chapter stems from the use of a new simplification approach to both achieve attractive net power generation levels and yield important insights into the underlying optimization problem. Specifically, we use a 3DOF model of the kite in spherical coordinates and linearize it around a zero-power circular cross-current equilibrium trajectory. This makes it possible to formulate power maximization as a simple indefinite quadratic optimal control problem with linear dynamic constraints. Expressing the kite's input trajectory in terms of sinusoidal perturbations from equilibrium makes it possible to translate this problem into an even simpler static indefinite quadratic program. We use traditional linear quadratic regulation to force the nonlinear kite dynamics to track the solution to this linearized problem. This approach furnishes a very attractive net power generation level, considering its simplicity, with a Loyd factor approaching 20%. Moreover, the approach yields important insights into the nature of the optimal trajectory, one example being the degree to which reel-out and reel-in are achieved in the plane perpendicular to the free-stream flow. The remainder of the chapter: presents the kite model; formulates and solves the kite trajectory optimization problem; then finally simulates the nonlinear kite model and examines its performance as it tracks the trajectory generated by the simplified linear analysis. This contribution was submitted to the IEEE Control Systems Letters and to to the American Control Conference and is currently in review. [34].

3.2 Kite Model

In this section we use the model we derived in Chapter 2 but with some modifications needed for our analysis. Similar to Chapter 2 the model assumes that the kite's attitude dynamics (roll, pitch, and yaw) can be controlled by lower-level controllers to track a desired attitude trajectory accurately. This allows the higher-level optimization work in this chapter to focus on the translational dynamics of the kite, represented as a point mass. In solving this optimization problem, we treat the kite's angle of attack, induced roll (or banking) angle, and tether tension as control inputs that can be manipulated to achieve a desired translation trajectory. Additionally, we assume that the kite is neutrally buoyant, meaning that its weight cancels with the buoyancy force. In this chapter, however, we examine the special case where the kite's anchor point is immersed underwater at a sufficient depth to allow the kite to fly in a circular, zero-power cross-current equilibrium trajectory centered directly downstream of this anchor point. We use this reference trajectory as a starting point for linearizing the kite's dynamics. This assumption places some limitations on the kite's anchoring system, but makes it possible to obtain important analytic insights into the nature of the optimal kite trajectory.

The kite's underwater motion is governed by the forces acting on it, namely, the: gravitational, tension, buoyancy, and hydrodynamic surface forces. The hydrodynamic surface forces are typically decomposed into lift, drag, and side force. We define a spherical coordinate frame $\mathscr{S}$ with unit vectors: $\{\hat{e}_r, \hat{e}_\theta, \hat{e}_\psi\}$. We can relate this frame to a Cartesian frame as shown in Figure 3.1. We can write the position

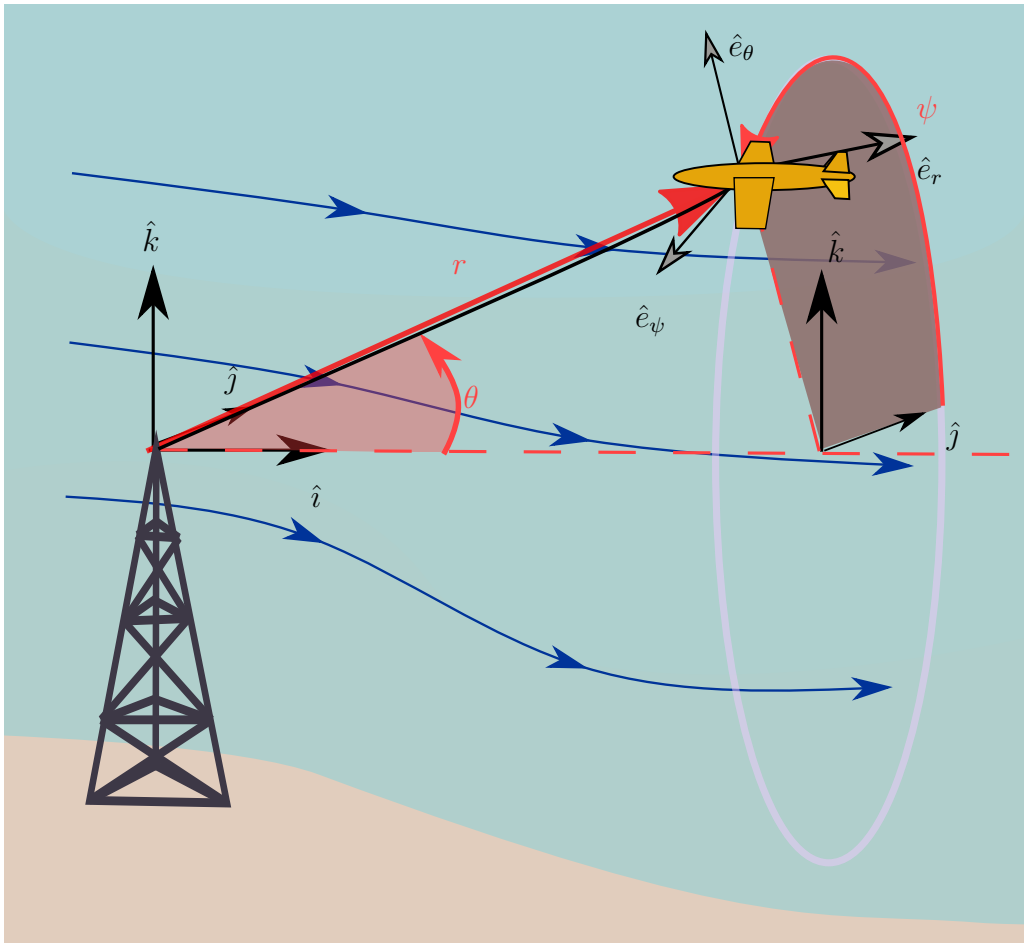

Figure 3.1: Underwater kite with unit vectors in Cartesian and spherical coordinates

vector and its derivatives:

$$\boldsymbol{r} = r\hat{e_r} \tag{3.1}$$

$$\dot{\boldsymbol{r}} = \dot{r}\hat{e_r} + r\dot{\theta}\hat{e}_\theta + r\dot{\psi}\sin\theta\hat{e}_\psi \tag{3.2}$$

$$\begin{aligned}\ddot{\boldsymbol{r}} = &\left(\ddot{r} - r\dot{\theta}^2 - r\dot{\psi}^2\sin\theta\sin\theta\right)\hat{e}_r \\ &+ \left(\dot{r}\dot{\theta} + r\ddot{\theta} - r\dot{\psi}^2\sin\theta\cos\theta\right)\hat{e}_\theta \\ &+ \left(\dot{r}\dot{\psi}\sin\theta + r\ddot{\psi}\sin\theta + r\dot{\psi}\dot{\theta}\cos\theta\right)\hat{e}_\psi\end{aligned} \tag{3.3}$$

We can now write an expression for the relative velocity of the kite with respect to the fluid. We define the velocity of the water along the $\hat{\imath}$ direction: $\boldsymbol{V_w} = u_w\hat{\imath}$. In spherical coordinates this becomes $\boldsymbol{V_w} = u_w \cos\theta \hat{e}_r - u_w \sin\theta \hat{e}_\theta$. The relative velocity is thus:

$$\boldsymbol{V_{rel}} = \dot{\boldsymbol{r}} - \boldsymbol{V_w} \tag{3.4}$$

$$\boldsymbol{V_{rel}} = (\dot{r} - u_w \cos\theta)\,\hat{e_r} + \left(r\dot{\theta} + u_w \sin\theta\right)\hat{e}_\theta + r\dot{\psi}\sin\theta\hat{e}_\psi \tag{3.5}$$

Let us define a new frame $\mathscr{W}$ with respect to which we will define the external forces applied to this kite.

$$\hat{x}_w = \frac{\boldsymbol{V_{rel}}}{|\boldsymbol{V_{rel}}|}, \qquad \hat{z}_w = \frac{\hat{x}_w \times \boldsymbol{r}}{|\hat{x}_w \times \boldsymbol{r}|}, \hat{y}_w = \frac{\hat{z}_w \times \hat{x}_w}{|\hat{z}_w \times \hat{x}_w|} \tag{3.6}$$

The forces the kite experiences are:

$$\boldsymbol{L} = \frac{1}{2}\rho S C_L(\alpha)|\boldsymbol{V_{rel}}|^2(cos(\phi)\hat{y}_w + sin(\phi)\hat{z}_w) \tag{3.7}$$

$$\boldsymbol{D} = -\frac{1}{2}\rho S C_D(\alpha)|\boldsymbol{V_{rel}}|^2\hat{x}_w \tag{3.8}$$

$$\boldsymbol{T} = T\frac{\boldsymbol{r}}{|\boldsymbol{r}|} \tag{3.9}$$

These are illustrated in Figure 3.2. where T, α, ϕ are the scalar tension force (always

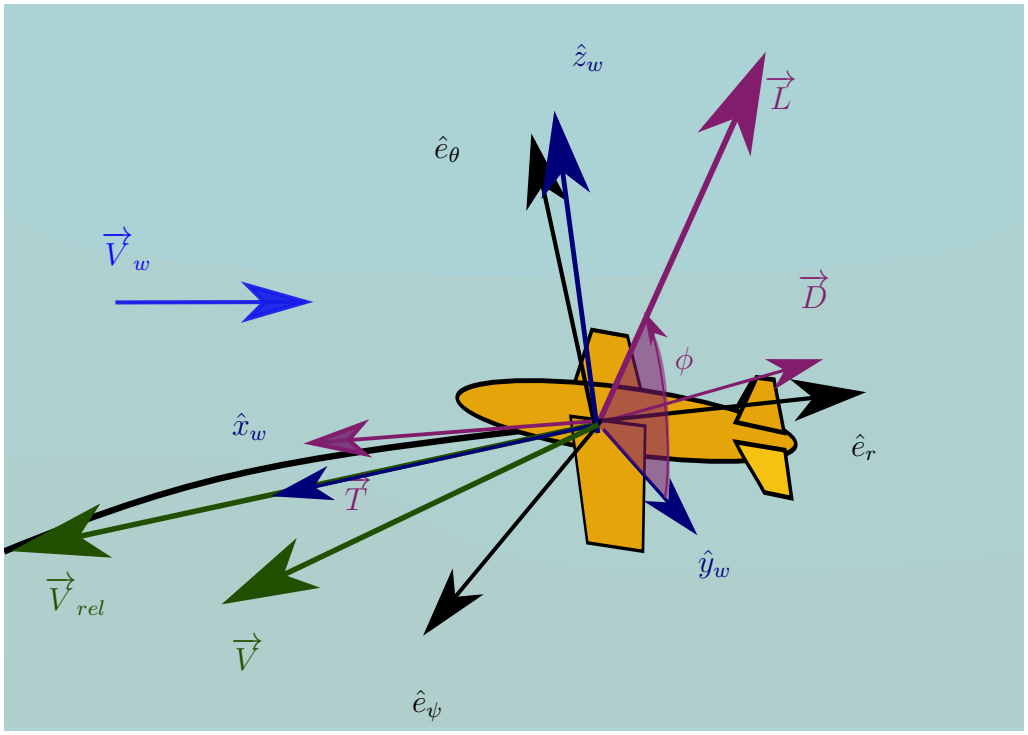

Figure 3.2: Water frame and external forces

negative), the angle of attack, and the roll angle, respectively. The other parameters $\rho, C_L, C_D,$ and S are, respectively, the water density, the lift coefficient, the drag coefficient, and the wing area. The hydrodynamic coefficients C_L and C_D are modeled in terms of α as follows:

$$C_L(\alpha) = c_1\alpha + c_2 \tag{3.10}$$

$$C_D(\alpha) = b_1\alpha^2 + b_2\alpha + b_3 \tag{3.11}$$

The equations of motion for this kite are thus given by:

$$m\ddot{\boldsymbol{r}} = \sum \boldsymbol{F_{ext}} \tag{3.12}$$

where $\sum \boldsymbol{F_{ext}} = \boldsymbol{L} + \boldsymbol{D} + \boldsymbol{T}$.

We express the above equations of motion in state-space form, with two important caveats. First, we note that in the absence of flow shear (i.e., if free-stream water velocity is spatially uniform), we do not need to include ψ as a state variable in the model. This makes it possible to represent a zero-power circular trajectory perpendicular to the free-stream flow as a single equilibrium point in the kite's state space. Our optimization study utilizes a dynamic model linearized around this equilibrium. Second, to ensure a smooth trajectory, our optimization problem penalizes the rates of change of the kite's angle of attack α, induced roll angle ϕ, and tension T. To allow for such a penalty within a standard optimal control problem formulation, we make the rates of change of these three variables control inputs. This leads to a state-space model of the form below:

$$\frac{d}{dt}X = f(X, U) \tag{3.13}$$

where $X = \begin{bmatrix} r & \theta & v & p & q & T & \alpha & \phi \end{bmatrix}^T$, $U = \begin{bmatrix} u_1 & u_2 & u_3 \end{bmatrix}^T$, and:

$$f(X,U) = \begin{bmatrix} v \\ p \\ \frac{\boldsymbol{F}}{m} \cdot \hat{e}_r + rp^2 + rq^2 \sin\theta^2 \\ \frac{1}{r}\left(\frac{\boldsymbol{F}}{m} \cdot \hat{e}_\theta - vp + rq^2 \sin\theta\cos\theta\right) \\ \frac{1}{r\sin\theta}\left(\frac{\boldsymbol{F}}{m} \cdot \hat{e}_\psi - vq\sin\theta - rqp\cos\theta\right) \\ u_1 \\ u_2 \\ u_3 \end{bmatrix} \tag{3.14}$$

3.3 Problem Formulation

3.3.1 Optimization Objective

We formulate a periodic kite trajectory optimization problem with the following structure:

$$\text{Minimize } J = \int_0^T L\left(X,U\right) dt \tag{3.15}$$

$$\text{Subject to: } \dot{X} = f\left(X,U\right), X(0) = X(T) \tag{3.16}$$

The objective function in this problem is given by $L(X,U) = -P + U^T R U$, where $P(t)$ is instantaneous mechanical power given by $P = -vT$ and $U^T R U$ is a positive-definite quadratic penalty on the control input vector. Thus, the optimiza-

tion objective reflects a desire to maximize cycle-averaged mechanical power with a penalty on the rates of change of the physical control inputs needed for doing so. The mechanical power term is positive when the kite harvests energy and negative when it is reeled in. Note that this power term can be written in quadratic form as $P = X^T Q X$, where the state vector X contains the kite velocity v and tether tension T, implying that the matrix Q is negative semi-definite. Therefore, the above optimization problem has a non-convex quadratic objective.

3.3.2 Model Linearization

Solving the above trajectory optimization problem is difficult due to its nonlinearity, non-convexity, and high dimensionality (with 8 state variables). The problem becomes much simpler if one solves it approximately in the neighborhood of a state-input pair, X_{eq}, U_{eq}, satisfying the definition of an equilibrium point, i.e.,

$$f(X_{eq}, U_{eq}) = \mathbf{0} \tag{3.17}$$

The kite has an infinite number of equilibria, corresponding to different circular trajectories in a plane perpendicular to the free-stream water velocity vector, with the centers of the circles aligned with the tether anchor point. For any given equilibrium, the kite's dynamics can be linearized to furnish:

$$\frac{d}{dt}\tilde{X} = A\tilde{X} + B\tilde{U} \tag{3.18}$$

where $\tilde{X}$ and $\tilde{U}$ represent state/input perturbations from equilibrium, $A = [\partial f / \partial X]_{eq}$,

and $B = [\partial f / \partial U]_{eq}$

3.3.3 Simplified Optimization Problem

Linearizing the dynamics of the kite around a reference equilibrium simplifies the above trajectory optimization problem significantly as follows:

$$\text{Minimize } J = \int_0^T L\left(X_{eq} + \tilde{X}, U_{eq} + \tilde{U}\right) dt \tag{3.19}$$

$$\text{Subject to: } \dot{\tilde{X}} = A\tilde{X} + B\tilde{U}, \tilde{X}(0) = \tilde{X}(T) \tag{3.20}$$

The above problem can be simplified further as follows. First, recall that the input vector $U(t)$ consists of the rates of change of the kite's angle of attack, roll angle, and tether tension. All three of these state variables are constant at equilibrium, meaning that the equilibrium input U_{eq} must equal zero. As a result, $U(t) = U_{eq} + \tilde{U}(t)$ must equal $\tilde{U}(t)$ and therefore the control input penalty simplifies to $\tilde{U}^T R \tilde{U}$. Second, since the tether release rate $v(t)$ must equal zero at equilibrium, one can conclude that $v(t) = v_{eq} + \tilde{v}(t)$ must equal $\tilde{v}(t)$. By definition, mechanical power is given by $P(t) = v(t)T(t) = (v_{eq} + \tilde{v}(t))(T_{eq} + \tilde{T}(t))$, a term that simplifies to $\tilde{v}(t)(T_{eq} + \tilde{T}(t))$. Furthermore, expressing the optimal periodic trajectory of $\tilde{v}(t)$ as a Fourier series leads to the conclusion that the cycle average of $\tilde{v}(t)T_{eq}$ is zero. Combining all of these insights leads to the following simplified trajectory optimization problem statement:

$$\text{Min. } J = \int_0^T L\left(\tilde{X}, \tilde{U}\right) dt = \int_0^T \tilde{X}^T Q \tilde{X} + \tilde{U}^R Q \tilde{U} dt \tag{3.21}$$

$$\text{Subject to: } \dot{\tilde{X}} = A\tilde{X} + B\tilde{U}, \tilde{X}(0) = \tilde{X}(T) \tag{3.22}$$

3.3.4 Analytical Solution

The above simplified trajectory optimization problem has linear dynamics and a non-convex objective, thanks to the fact that the matrix Q is negative semi-definite. As a result, this problem's solution is unbounded in terms of the magnitudes of the optimal state and input perturbations $\tilde{X}$ and $\tilde{U}$, respectively. In practice, the optimal kite trajectory is bounded by space constraints as well as the diminishing accuracy of the above linearized kite model for larger motion magnitudes. With this in mind, we analyze the structure of the problem for a sinusoidal input trajectory of the form:

$$\tilde{U}(t) = \boldsymbol{u_1} \sin \omega t + \boldsymbol{u_2} \cos \omega t \tag{3.23}$$

where ω is the frequency of the sinusoidal trajectory, and the coefficients $\boldsymbol{u_1}$ and $\boldsymbol{u_2}$ are assumed to be small. With a sinusoidal input trajectory and linear dynamics we can analytically obtain an expression for the state variables as a function of time. The linear dynamics of the system are represented by the transfer function of the

system $G(s)$ in the Laplace domain.

$$G(s) = [sI - A]^{-1} B \tag{3.24}$$

We can now write an analytical expression for our state variables as a function of time as follows:

$$\tilde{X}(t) = (G_r \boldsymbol{u_1} - G_i \boldsymbol{u_2}) \sin \omega t + (G_i \boldsymbol{u_1} + G_r \boldsymbol{u_2}) \cos \omega t \tag{3.25}$$

where G_r and G_i are the real and imaginary components of $G(s)|_{s=j\omega}$. Notice that the transfer function enforces the dynamic constraint in our linearized optimization problem. Moreover, the focus on the steady-state response to a sinusoidal input trajectory ensures periodicity.

We can substitute expressions (3.23) and (3.25) into the objective (3.19) and obtain a static optimization problem where the optimization variables are the vectors $\boldsymbol{u_1}$ and $\boldsymbol{u_2}$.We can thus re-write the optimization problem. After linearizing the dynamics of the system and imposing a sinusoidal input trajectory our optimization problem becomes an unconstrained static quadratic optimization problem.

$$\text{Minimize} \quad J = \frac{\pi}{2\omega} \begin{bmatrix} \boldsymbol{u_1} & \boldsymbol{u_2} \end{bmatrix} \Phi_{6\times 6} \begin{bmatrix} \boldsymbol{u_1} \\ \\ \boldsymbol{u_2} \end{bmatrix} \tag{3.26}$$

where

$$\Phi_{[1:3,1:3]} = \Phi_{[3:6,3:6]} = R + G_r^T Q G_r + G_i^T Q G_i \tag{3.27}$$

$$\Phi_{[1:3,3:6]} = \Phi_{[3:6,1:3]} = [0]_{3\times 3} \tag{3.28}$$

The matrix Φ is indefinite, suggesting that the solution to this problem is unbounded. To better understand the structure of this solution, we focus on the particular direction in the optimization space that yields the fastest decrease in the minimization objective. In other words, we focus on the eigenvector of the matrix Φ associated with its most negative eigenvalue. Denoting this eigenvector by $\boldsymbol{v}$, we select:

$$\begin{bmatrix} \boldsymbol{u_1} \\ \\ \boldsymbol{u_2} \end{bmatrix} = \lambda \boldsymbol{v} \tag{3.29}$$

where λ is a scaling gain. In the linearized optimization problem, increasing this gain to infinity always yields benefits, at the expense of increasing departure from the true nonlinear dynamics. This motivates the final step in our analysis, where we use linear quadratic regulation to enable the nonlinear kite dynamics to track the above optimal trajectory for different values of λ, thereby gaining insight into the practical limitations on the magnitude of λ.

3.4 Results

3.4.1 Performance Metric

To evaluate the performance of our control approach we can compare the average power the kite generates to the maximum theoretical power it can generate – namely, Loyd's limit. We will call the ratio of these quantities the Loyd factor. The Loyd limit [35] is defined as:

$$P = \frac{2}{27}\rho S u_{\mathrm{w}}^3 C_{\mathrm{L}} \left(\frac{C_{\mathrm{L}}}{C_{\mathrm{D}}}\right)^2 \tag{3.30}$$

3.4.2 Kite Linear Quadratic Regulator

The state and input trajectories generated in the previous sections assume that the dynamics of the kite are linear. The further the kite's trajectory deviates from equilibrium, the less this assumption is valid. We propose to use the obtained trajectories as a reference to a linear-quadratic regulator. We then simulate the non-linear kite model as it attempts to track this reference.

We formulate the LQR problem as follows:

$$\text{Minimize } J = \int_0^\infty (X_{error}^T Q_{LQR} X_{LQR}^T + U^T R_{LQR} U) dt \tag{3.31}$$

$$\text{Subject to: } \dot{X}_{error} = AX_{error} + BU \tag{3.32}$$

This problem has a steady-state solution of the form:

$$U = -K_{LQR} X_{error} \tag{3.33}$$

The feedback gain matrix K_{LQR} will depend on Q_{LQR}, R_{LQR}, A and B.

3.4.3 Numerical Simulation

To evaluate our control strategy we simulate a non-linear kite as it tracks the reference sinusoidal trajectory obtained in the previous section. To avoid large control inputs at initialization, we start the kite at equilibrium and gradually increase the magnitude of the reference trajectory. Table 3.1 contains the parameters used for the simulation.

Figure 3.3 shows the position trajectory of the kite for the last 3 periods of simulation. One interesting feature of this result is that the kite reels away by mostly moving cross-current instead of parallel to the flow. In fact, the kite's downstream distance from the tether anchor point experiences relatively modest changes, with much of the reel-in and reel-out action occurring "in plane". One possible explanation is the degree to which the kite's fast cross-current motion makes such an oval in-plane trajectory both feasible and attractive. This is an important insight, and not necessarily an intuitive one compared to a trajectory where reel-in and reel-out occur along the free-stream flow direction.

Figures 3.4 and 3.5 show the power, release rate, and tension trajectories for the linear and non-linear kite models. The average power of the non-linear kite for

Kite Parameters			
Mass	m	2700	kg
Wing reference area	S	10	m^2
Aerodynamic coefficients	c_1	6.25e−2	deg^{-1}
	c_2	1.33e−1	-
	b_1	2.442e−4	deg^{-2}
	b_2	1.06e−3	deg^{-1}
	b_3	2.22e−3	-
Flow Parameters			
Water density	ρ	1000	kg/m^3
Water speed	u_w	1	m/s
Optimization Parameters			
Input quadratic penalties	R_{11}	0	-
	R_{22}	10e9	-
	R_{33}	30e9	-
Controller Parameters			
	q_{11}	2e12	-
	q_{22}	2e12	-
	q_{33}	2e12	-
	q_{44}	2e14	-
	q_{55}	2e13	-
	q_{66}	2e2	-
	q_{77}	2e2	-
	q_{88}	2e−1	-
	q_{99}	2e11	-
	r_{11}	1e−6	-
	r_{22}	1e8	-
	r_{33}	2e10	-

Table 3.1: Parameters

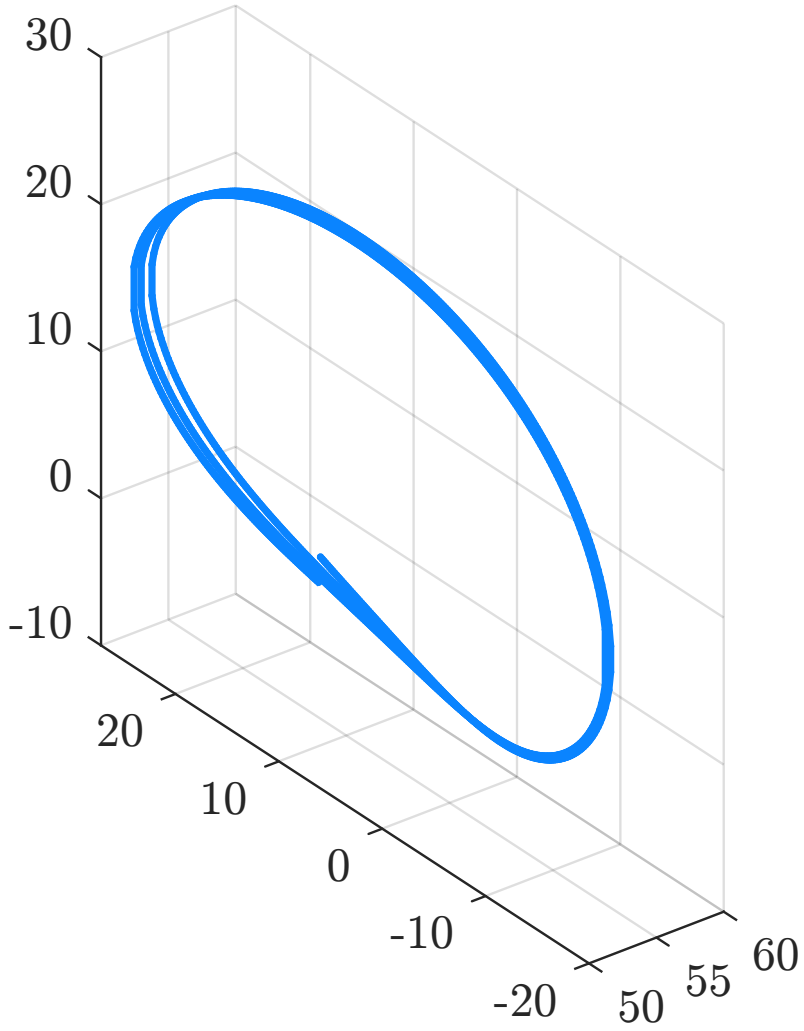

Figure 3.3: Path of the non-linear kite model in the last 3 periods of simulation

this simulation is 16.4kW which corresponds to Loyd factor of 19.9%. This is an attractive outcome, particularly in light of the simplicity of the approach used for achieving it.

3.4.4 Sensitivity to eigenvector scaling

Finally we explore how changing the scaling factor λ affects the generated power in these simulations. For this, we keep all parameters equal and do a sweep on the scaling factor λ. Figure 3.6 shows the average power generated by the non-

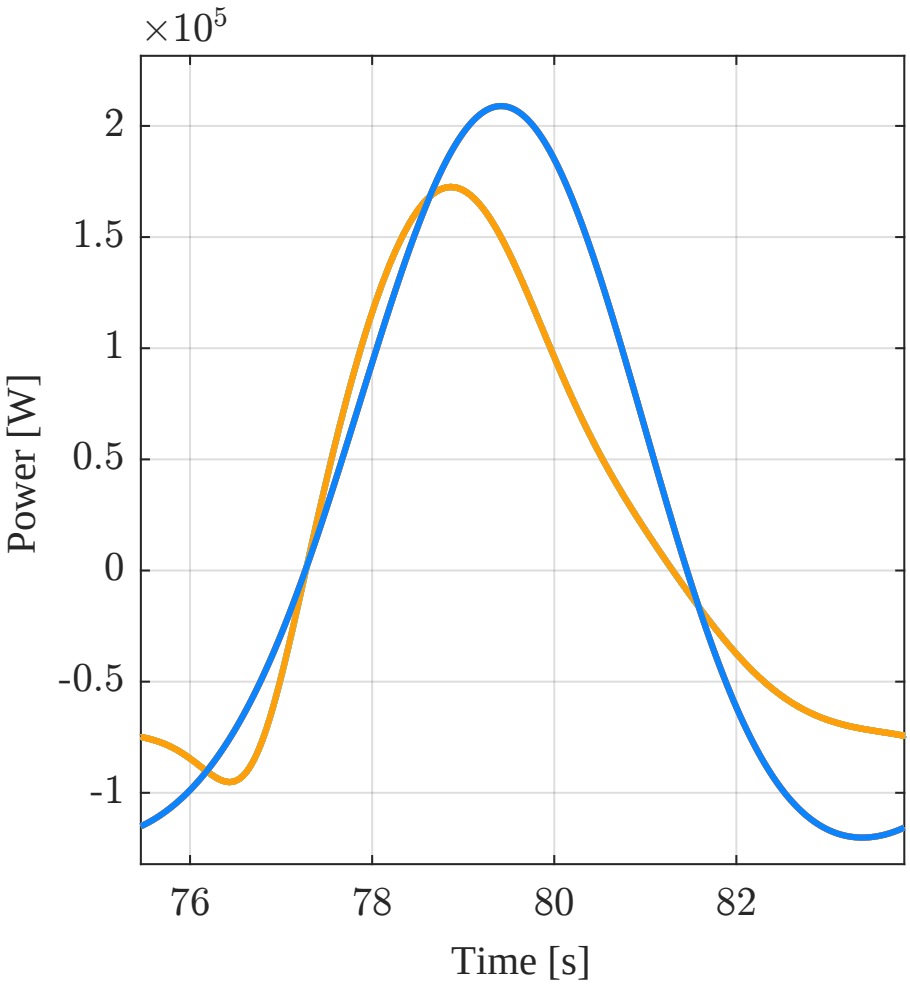

Figure 3.4: Power generated in the last period of simulation.Orange line: Non-linear model, Blue line: Linear model.

linear model in the vertical axis and the average power generated by the linear model in the horizontal axis as the scaling factor λ increases. The increasing scaling factor corresponds to larger deviations from equilibrium and the power generated by the non-linear model decreases in comparison to the linear one for increasing deviations. This places a practical limitation on how far one can "push" the solution of this trajectory optimization problem, even if the underlying simplified linear analysis leads to an unbounded solution.

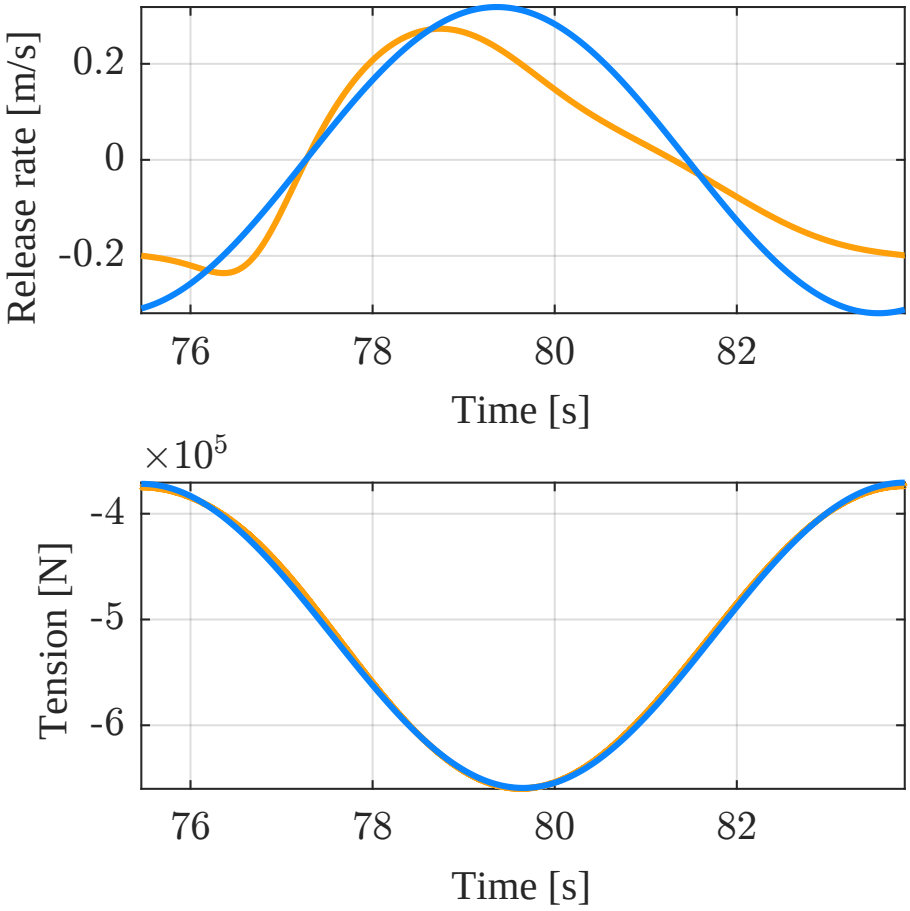

Figure 3.5: Release rate and tension for the last period of simulation. Orange line: Non-linear model, Blue line: Linear model.

3.5 Chapter conclusion

In this chapter we proposed to maximize the power generated by an underwater kite that operates in pumping mode. For this we derive a simplified 3DOF nonlinear kite model and formulate an optimization problem to maximize the mechanical power of the kite while minimizing the inputs. By performing simplifications such as linearizing the kite model and imposing a sinusoidal input trajectory we are able to transform a dynamic quadratic optimization problem into an unconstrained static optimization problem. We use the objective of this problem to obtain trajectories

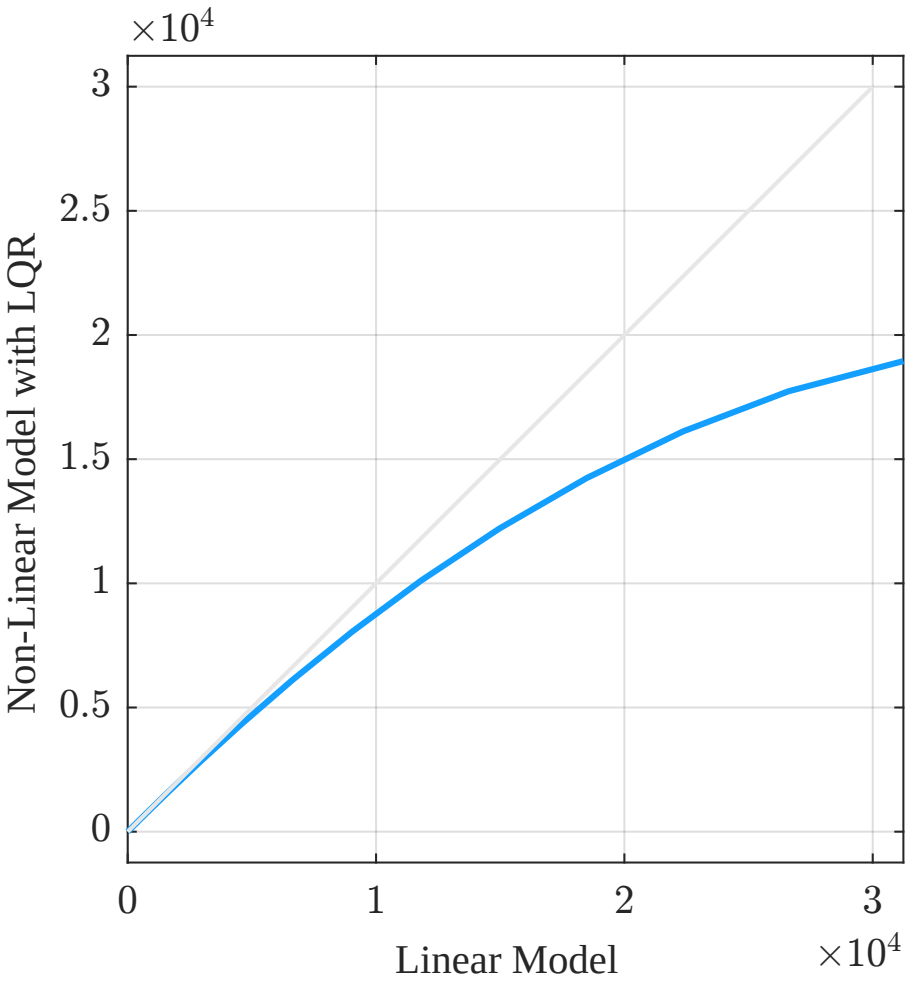

Figure 3.6: Average power generated by non-linear model vs. average power generated by linear model as the scaling factor λ increases

along its steepest direction of descent. By introducing a scaling factor we are able to adjust how much we deviate from the equilibrium of the system. The resulting trajectories were then tracked by a non-linear kite with a linear quadratic regulator. For a $1\mathrm{m\,s^{-1}}$ flow speed and a kite with a wing area of $10\mathrm{m}^2$ we generated an average power of 16.4kW corresponding to a Loyd factor of 19.9%. An increase in the scaling factor increases the generated power with decreasing gains as the trajectories depart further from equilibrium. One important insight we learned in this chapter is the degree to which reel-out and reel-in are achieved in the plane perpendicular to the

free-stream flow. This analysis neglects the electrical efficiencies of the system. In the next chapter we explored the effect introducing these has in our results.

Chapter 4: Modeling and Trajectory Generation with Electrical and Mechanical Losses

4.1 Chapter introduction

In the previous chapter we obtained trajectories optimized for mechanical power, these trajectories, however do not take into account the losses in the system. In this chapter we attempt to model these losses and take them into account in our trajectory generation strategy. For airborne kite system Stuyts et al. [28] explored the effect the electrical conversion efficiency has on the optimal cycles. In this chapter we explore the same effect on our optimization approach for underwater kites.

4.2 Modeling of the electric machine

There are different modeling approaches for electric motors with different levels of fidelity [36]. In the context of optimization we neglect the high frequency dynamics of the motor and consider a linear model that bundles iron and copper losses of the motor into a resistance value, and all the mechanical friction with a single friction coefficient proportional to the angular speed of the motor shaft.

We can write the dynamics of a DC motor in state space formulation as follows:

$$\frac{d}{dt}\begin{bmatrix}\omega \\ i\end{bmatrix} = \begin{bmatrix}-\frac{b}{J} & \frac{K}{J} \\ -\frac{K}{L} & -\frac{R}{L}\end{bmatrix}\begin{bmatrix}\omega \\ i\end{bmatrix} + \begin{bmatrix}0 & \frac{1}{J} \\ \frac{1}{L} & 0\end{bmatrix}\begin{bmatrix}V & \tau\end{bmatrix} \tag{4.1}$$

where ω,i, τ and V are the motor angular speed, the armature current, external torque, and armature voltage respectively. The parameters b, J, K, L, and R are the friction coefficient, the motor inertia, the motor constant, the motor inductance and the armature resistance. We expect the dynamics of the kite to be much slower than the dynamics of the electric motor. We can thus reduce the order of this model by evaluating it at steady state.

At steady state:

$$\frac{d}{dt}\begin{bmatrix}\omega \\ i\end{bmatrix} = \mathbf{0} \tag{4.2}$$

and we can write an expression for the current i and voltage V as follows:

$$i = \frac{1}{K}(\tau + b\omega) \tag{4.3}$$

$$V = K\omega + \frac{R}{K}(\tau + b\omega) \tag{4.4}$$

We can re-write these expressions in terms of the tether tension and tether release rate by accounting for the spool radius

$$i = \frac{1}{K}(Tr + b\frac{v}{r}) \tag{4.5}$$

$$V = K\frac{v}{r} + \frac{R}{K}(Tr + b\frac{v}{r}) \tag{4.6}$$

where T, v and r are the tether tension, tether release rate and spool radius respectively.

4.3 Problem formulation

We can use the expressions obtained in the previous section to write an expression for the electric power the motor generates as follows:

$$P_{elec} = Vi \tag{4.7}$$

$$P_{elec} = (K\frac{v}{r} + \frac{R}{K}(Tr + b\frac{v}{r}))\frac{1}{K}(Tr + b\frac{v}{r}) \tag{4.8}$$

$$\tag{4.9}$$

Notice that T and r are state variables in our model in Chapter 3. Furthermore they appear quadratically in the expression for electric power. This makes it possible to re-write our optimization objective from Chapter 3 as follows:

$$\text{Minimize } J = \int_0^T L\left(X, U\right) dt \tag{4.10}$$

$$\text{Subject to: } \dot{X} = f\left(X, U\right), X(0) = X(T) \tag{4.11}$$

where this time the objective function becomes $L(X, U) = -P_{elec} + U^T RU$, where $P_{elec}(t)$ is the instantaneous electrical power given by 4.9 and $U^T RU$ is the same positive-definite quadratic penalty on the control input vector we introduced in Chapter 3. Thus, the optimization objective reflects a desire to maximize cycle-averaged electrical power with a penalty on the rates of change of the physical control inputs needed for doing so. Again, this power term can be written in quadratic form as $P = X^T Q_{elec} X$, where the state vector X contains the tether release rate v and tether tension T.

We can follow the same procedure we followed in Chapter 3 to analytically obtain sinusoidal trajectories that scaled proportionally to the eigenvector along the power maximizing direction of our objective.

4.4 Simulation & Results

We parametrize our model with the parameters of our lake-test setup. This allows us to use real-world parameters that are consistent with the experiments we performed. The parameters for the simulation are given in Table 4.1.

One challenge in generating trajectories for the scale of our experimental setup

is that we need to ensure that the tension and release rate trajectories are within the allowable range of operation of our experimental setup. While our methodology to generate the trajectories does not explicitly put bounds on the state variables or input variables, we can scale these by scaling the amplitude of the trajectories proportionally to the eigenvector along the direction that maximizes power. Additionally we can select the equilibrium value for some of our state variables– along which we linearize our system– to be within the range of operation of our machine. The equilibrium conditions are:

$$X_0 = \begin{bmatrix} 30 & 0.15 & 0 & 0 & -0.547 & -200 & -0.0205 & 0.6793 \end{bmatrix}^T \tag{4.12}$$

To compare the trajectories we generate optimizing for mechanical power and the trajectories we generate optimizing for electrical power, we scale the eigenvector such that the average mechanical power both generate is equal. The release rate and tension trajectories we obtain for the linear model for a duration of three periods are shown in Figure 4.1.

The electric power trajectory generated by these is given in Figure 4.2.

Similar to what we did in Chapter 3 we can track these trajectory with an LQR controller to assess the validity of these results for the non-linear kite model. Figure 4.3 shows the release rate and tension trajectory a non-linear model of the kite follows by tracking the trajectory optimized for electric power in Figure 4.1. The resulting path the kite follows is shown in Figure 4.4.

Table 4.2 summarizes the results in terms of the average mechanical power

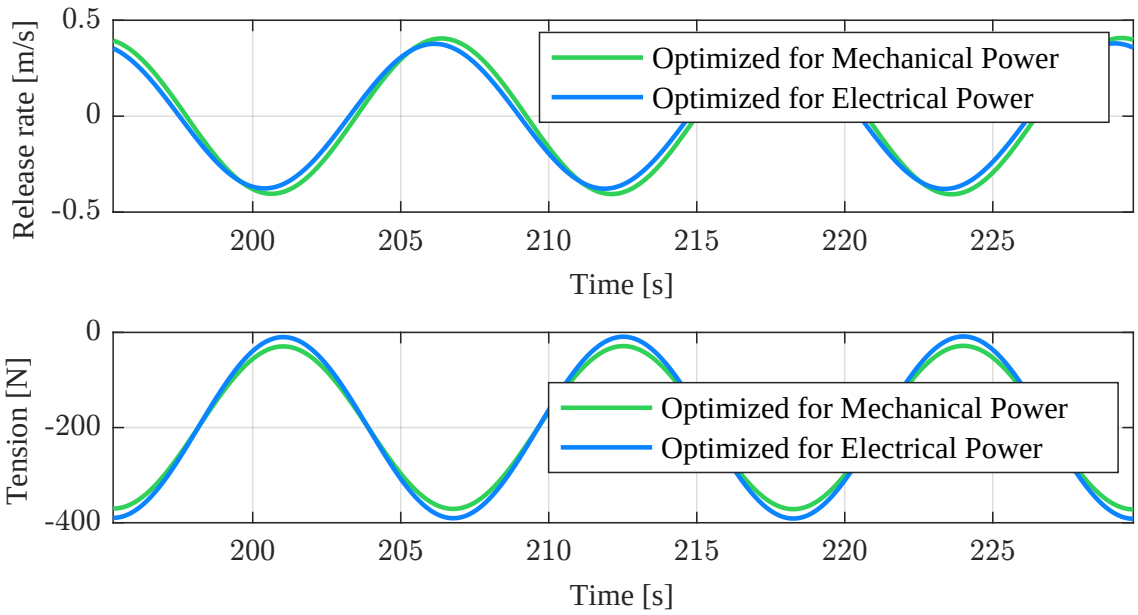

Figure 4.1: Release rate and tension trajectories by optimizing for mechanical and electrical power — Linearized model

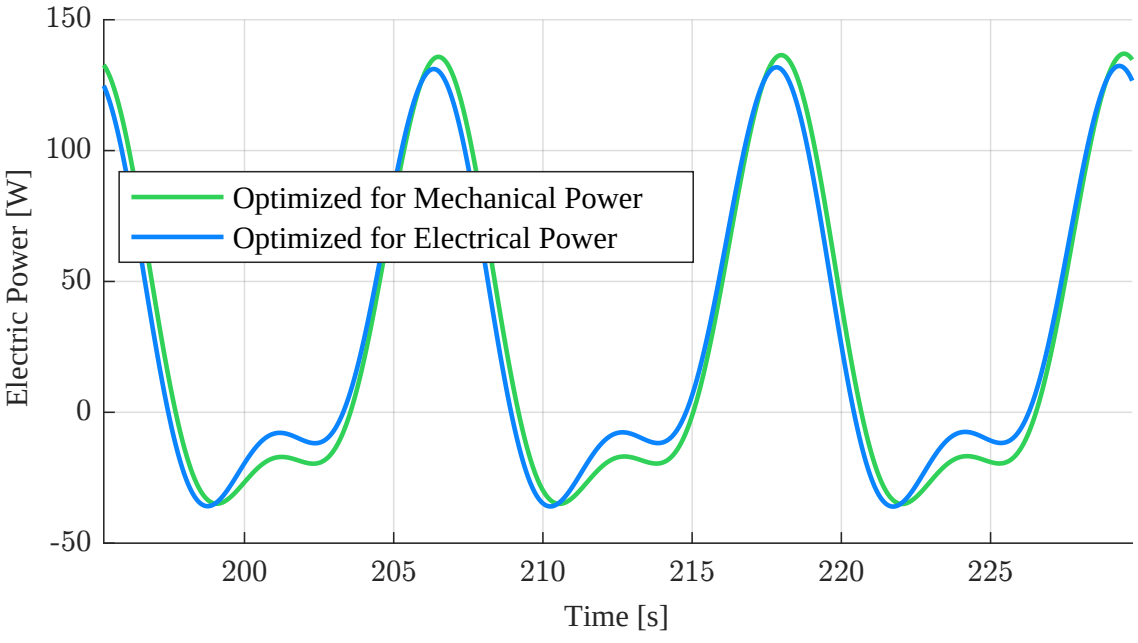

Figure 4.2: Electric power trajectories by optimizing for mechanical and electrical power

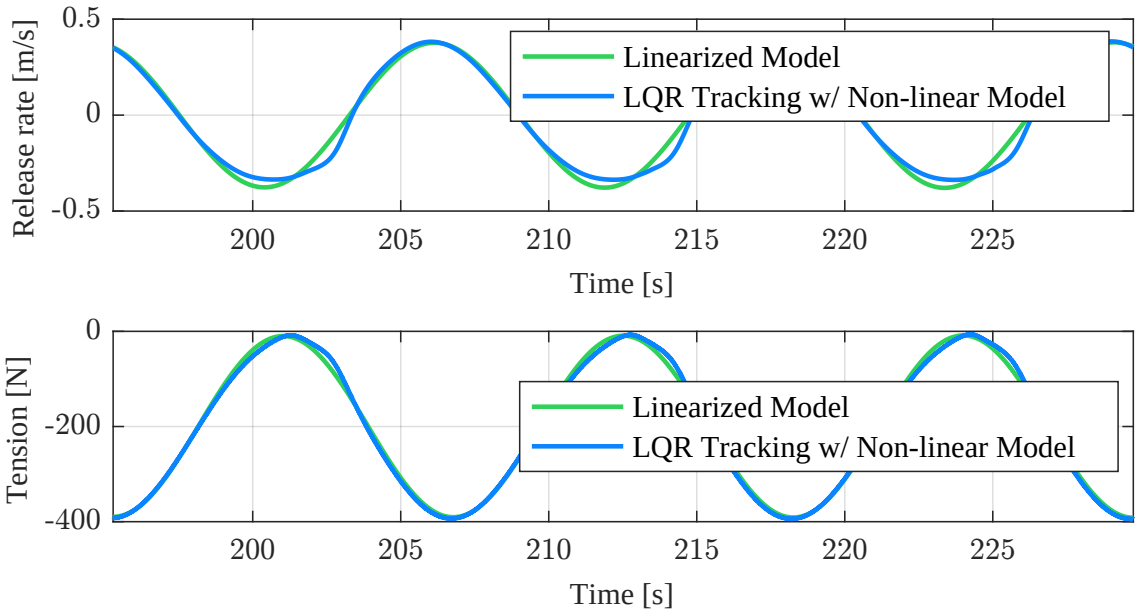

Figure 4.3: Release rate and tension trajectories optimized for electrical power and tracked by LQR controller.

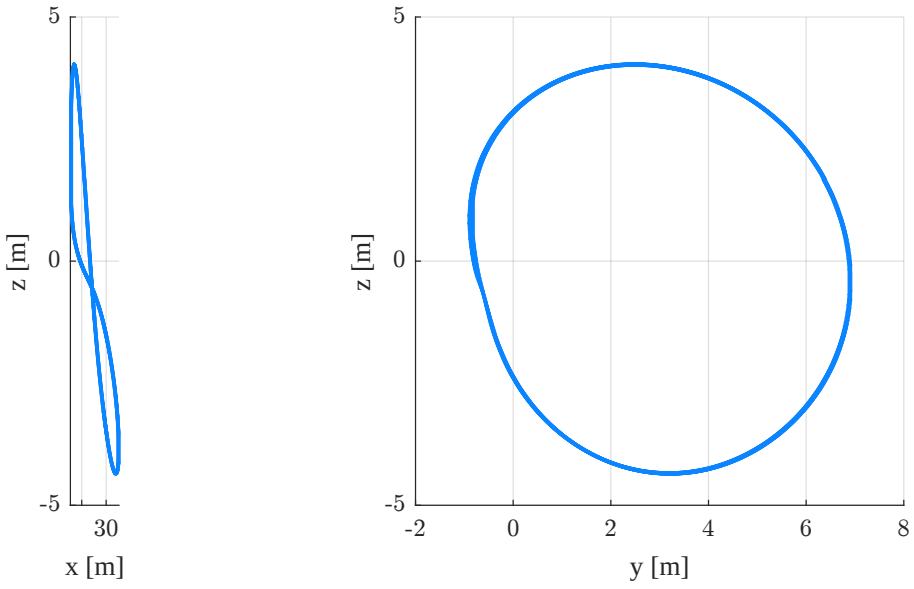

(a) Lateral view (b) Front view

Figure 4.4: Kite path in Cartesian coordinates

and electrical power the different trajectories generate.

4.5 Chapter conclusion

In this chapter we derived a simplified dc-motor model and integrated into the trajectory generation framework we developed in chapter 3. We empirically parametrized our model and compared the solution to the problem that incorporates the system losses into the optimization objective with the solution that neglects them. The average electric power generated by the trajectory that optimizes for electric power was larger than the trajectory that optimizes for mechanical power only, the difference however was almost negligible.

Kite Parameters			
Mass	m	100	kg
Wing reference area	S	1	m^2
Aerodynamic coefficients	c_1	6.25e−2	deg^{-1}
	c_2	1.33e−1	-
	b_1	2.442e−4	deg^{-2}
	b_2	1.06e−3	deg^{-1}
	b_3	2.22e−3	-
Flow Parameters			
Water density	ρ	1000	$\mathrm{kg/m}^3$
Water speed	u_w	1	m/s
PTO System Parameters			
Motor armature resistance	R	0.15	Ω
Motor constant	K	83.8	$\mathrm{N\,m\,A}^{-1}$
Shaft friction coefficient	b	0.0001	$\mathrm{N\,m\,s\,rad}^{-1}$
Spool radius	r	0.05	m
Motor gear ratio	GR	30	-
Optimization Parameters			
Input quadratic penalties	R_{11}	0	-
	R_{22}	4e7	-
	R_{33}	1e7	-
Controller Parameters			
	q_{11}	2e12	-
	q_{22}	2e12	-
	q_{33}	2e12	-
	q_{44}	2e14	-
	q_{55}	2e13	-
	q_{66}	2e2	-
	q_{77}	2e2	-
	q_{88}	2e−1	-
	q_{99}	2e11	-
	r_{11}	1e−6	-
	r_{22}	1e8	-
	r_{33}	2e10	-

Table 4.1: Parameters

	Average Mechanical Power [W]	Average Electrical Power [W]
Linear Model Optimized for Mechanical Power	34.9	28.7
Linear Model Optimized for Electrical Power	34.9	28.9
LQR Tracking w/ Non-Linear Model	34.2	28.4

Table 4.2: Average power generated by different trajectories

Chapter 5: Design & Fabrication of Prototype Power Take-Off System for a Lab Scale MHK

5.1 Chapter introduction

This chapter deals with the design and fabrication of a laboratory setup to test the power take-off (PTO) system for an underwater kite. The work chapter 3 attempts to maximize the mechanical power of the MHK. This neglects both the mechanical losses and electrical losses that occur in the PTO. The setup discussed in this chapter allows us to experimentally evaluate our optimization results and quantify these system losses.

The power take-off (PTO) system converts the mechanical power of the kite into electrical power when acting as a generator. It also reels the kite in when acting as a motor. In the context of our collaboration with North Carolina State University, we designed and fabricated two PTO systems. One to be used as part of a suite of pool-tests where the kite would constantly reel-in. These test served as a preparation for a larger scale test to be performed at lake Norman in North Carolina. The second PTO is intended to perform both reel-in and reel-out in the lake. We designed and fabricated the PTO with the ability to perform laboratory

testing by utilizing two electric machines. While in the lake it is possible to use a single machine to both reel-in and reel-out, having the addition of a second machine provides the flexibility to test at higher power levels. In the laboratory one machine is used to simulate the tension generated by the kite, while the other acts as the PTO system. We are thus able to use this setup to replicate the trajectories we obtained in Chapter 3 in the lab.

5.2 Pool-test PTO

The first PTO we prototyped was meant to be used in motoring only, that is, without regeneration. The system consist of a tether spool, an encoder, and DC electric motor. The spool connects to a marine tether via a slip-ring, so that we can send power to the kite's control surface actuators, as well as electric signals such as actuator commands to the kite. Figure 5.1 describes the main components of the PTO, and a 3D CAD render is shown in Figure 5.2.Table 5.1 contains the list of components.

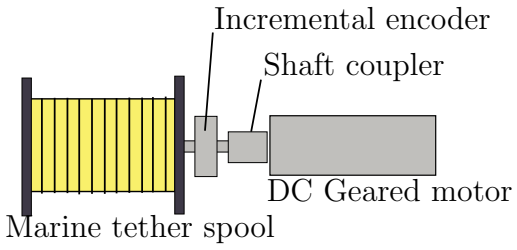

Figure 5.1: Description of PTO

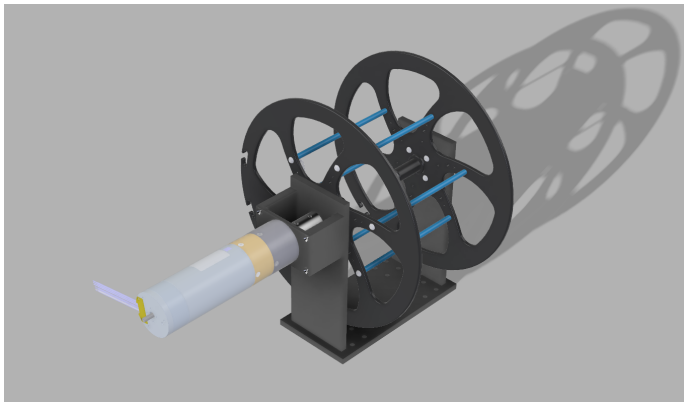

Figure 5.2: 3D CAD of PTO prototype

Supplier	Component
Digikey	48V Brushless DC Motor
Blue Robotics	Marine tether spool
Blue Robotics	Neutrally buoyant marine tether
Applied Motion Products	48V Motor controller
TRC Electronics	48V Power supply
Applied Motion Products	Incremental encoder

Table 5.1: Laboratory scale PTO components

The motor of the PTO is controlled by a DC motor controller. Moreover, we use an Arduino to interface the PTO with a Speedgoat real-time computer that provides the speed commands to the system. Figure 5.3 describes these connections.

This PTO was tested in an Olympic pool at North Carolina State University as shown in Figure 5.4 and served as a stepping stone for the development of the second PTO capable of regeneration.

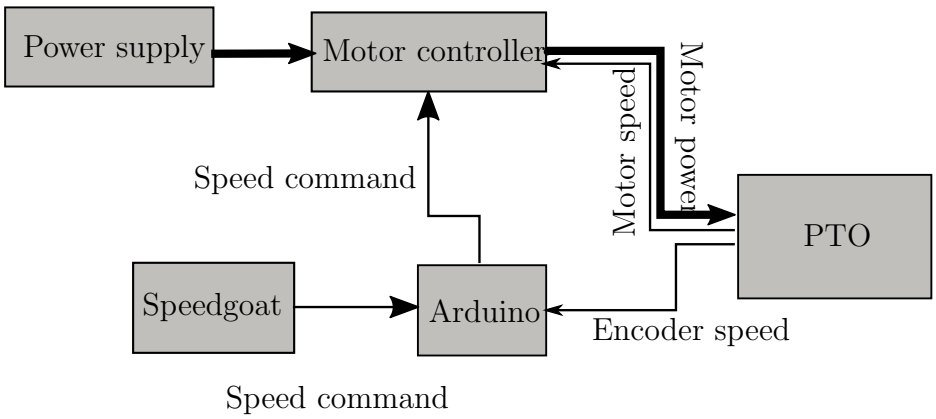

Figure 5.3: PTO connections diagram

5.3 Lake test PTO

Building upon the pool PTO we designed and fabricated a PTO system that was capable of regeneration. The most significant change between the pool and lake systems was the introduction of an additional shaft connected via a timing belt to the original shaft, allowing the simultaneous use of two electric machines. Having two electric machines instead of a single machine allows us to test at higher tension levels if necessary, but also allows for laboratory testing of the regeneration capabilities of the setup.

The lake test PTO used two of the 48V geared BLDC motors from the pool tests, controlled by a Roboteq HBL2360A motor controller. When used with a single electric machine the system is able to motor at a continuous tension of 400N at a speed of $0.5\mathrm{m\,s^{-1}}$. Figure 5.5 shows a diagram of the setup, and Figure 5.6 shows a

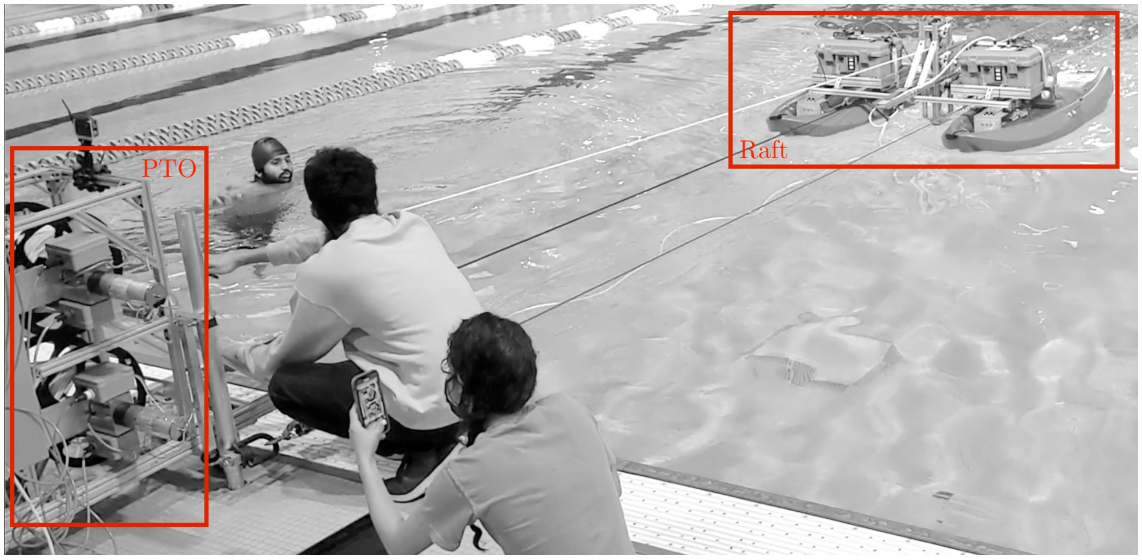

Figure 5.4: Picture of PTO pulling raft during pool testing

picture of the fabricated setup.

5.4 Laboratory Experiments

The capability for adding a second motor on the bottom shaft allows for testing in the laboratory before actual lake testing. This makes possible to assess the electrical power that it is expected to be generated by the trajectories we optimized.

To test the trajectories that we obtained in chapter 3 we scale down the tension trajectory so that it is within the allowable range of operation of the electric machines. The release-rate trajectory, however is left unchanged. To experimentally test our trajectories we command two different open-loop speed commands to the mechanically interconnected motors. Since the two motors are forced to spin at the same speed by the timing belt, one motor will be applying a torque on the other, if the speed commands differ. By increasing the difference in commanded speeds we can increase the torque one motor exerts on the other. We can relate torque and

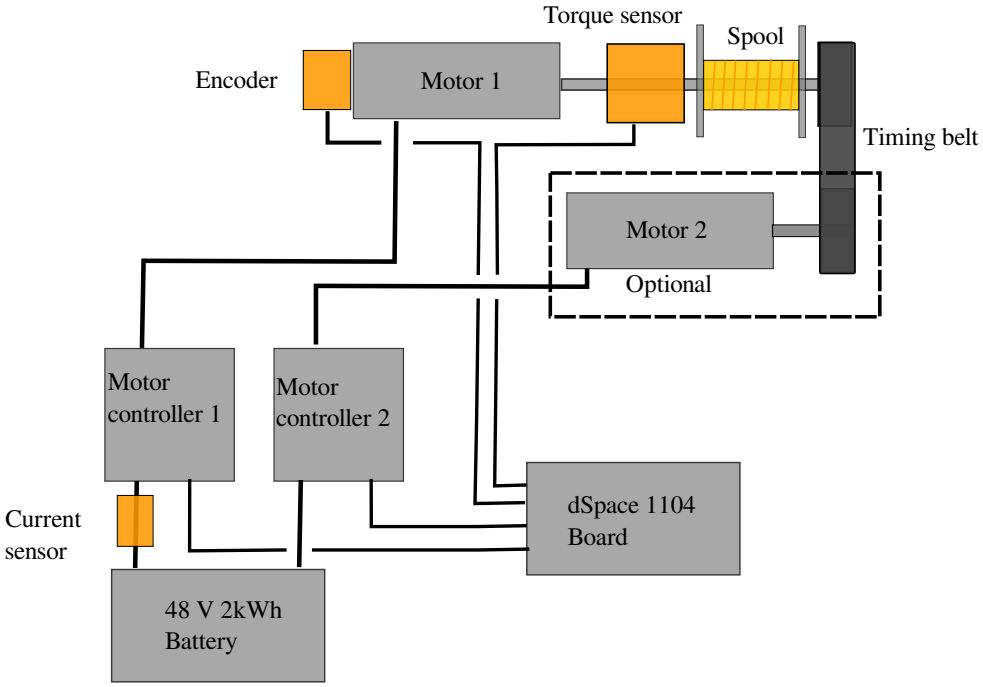

Figure 5.5: Diagram of PTO for lake test and its sensors.

angular speed to tension and release rate by taking into account the spool radius. Figure 5.7 shows the measured release rate and tension trajectories of the PTO. By measuring the torque at the output shaft of the motor, as well as its speed we can measure the mechanical power the top motor consumes when reeling-in and generates when reeling-out. By measuring the current going from the motor controller to the battery and the voltage of the battery we can measure the electrical power that is consumed or generated. We compare these power trajectories in Figure 5.8.

As expected the mechanical power is higher than the electrical power when reeling-out as our motor generates electricity, and the opposite occurs when reeling-in and the motor consumes electricity. This difference is caused by both the mechanical and electrical losses of the setup. We can integrate these trajectories to

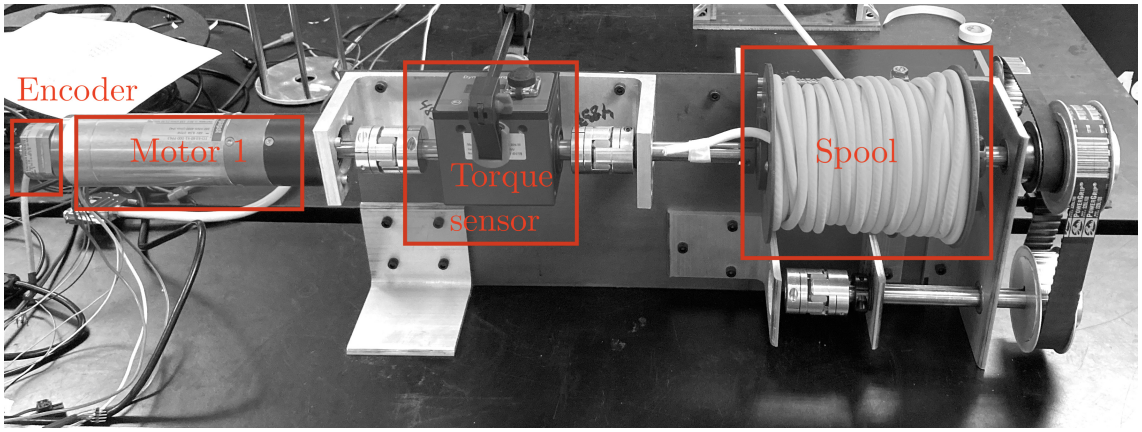

Figure 5.6: Picture of PTO for lake test that supports an additional motor on the bottom shaft.

see how much energy is produced, as shown in Figure 5.9. This figure illustrate how drastic is the difference in energy generated: An average mechanical power of 15.33W compared to an average electrical power of 0.16W.

5.5 Parameter identification

We use the experimental results presented in this chapter to estimate unknown parameters of the PTO system. Namely, we can estimate the armature resistance R, the damping coefficient b, and the motor constant K.

We estimate R and b using the loss in power after the electrical conversion as our measured variable. We can write an expression for the power loss assuming all the electric losses are captured by a linear function of current squared, and all the mechanical losses are captured by a linear function of the rotor speed squared:

$$P_{loss} = \|P_{mech} - P_{elec}\| = Ri^2 + b\omega^2 \tag{5.1}$$

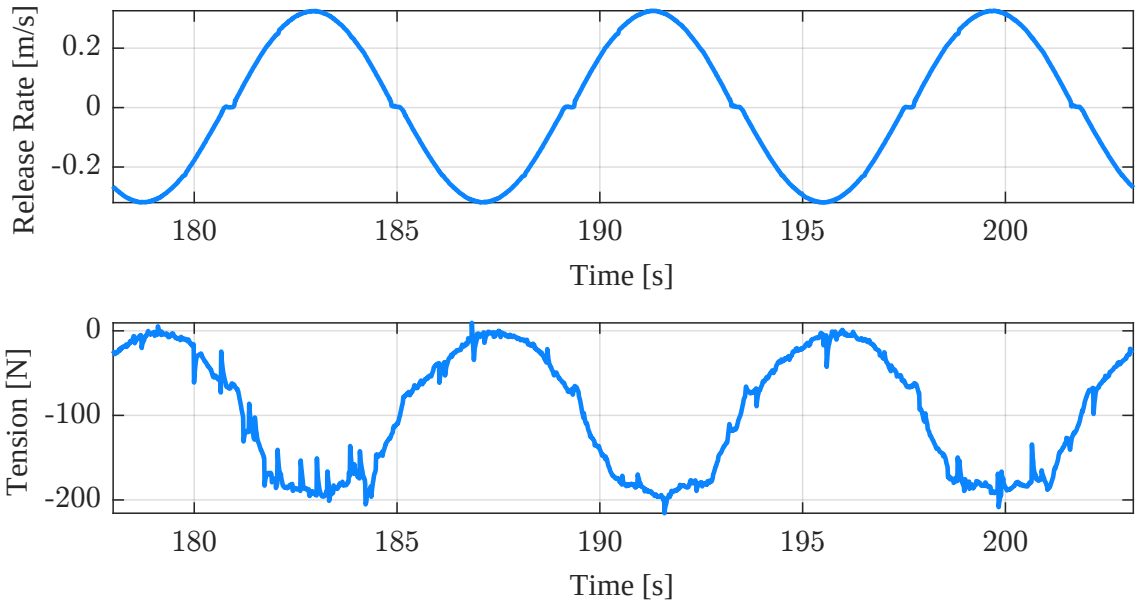

Figure 5.7: Measured release rate and tension during three periods.

	Parameter Estimate
Armature Resistance	4.939Ω
Damping Coefficient	$5.741\text{e}{-4}\,\text{N m rad}^{-1}\,\text{s}$
Motor Constant	$0.256\,\text{N m A}^{-1}$

Table 5.2: Parameter estimates

We can use this expression taking the current squared i^2 and the rotor speed squared ω^2 as regressors in a linear regression problem that we can solve using linear least squares.

We can perform the same technique to estimate the motor constant K by using as measured variable the motor torque τ and current as a regressor as torque and current are related linearly as:

$$\tau = Ki \tag{5.2}$$

The estimated parameters are shown in Table 5.2.

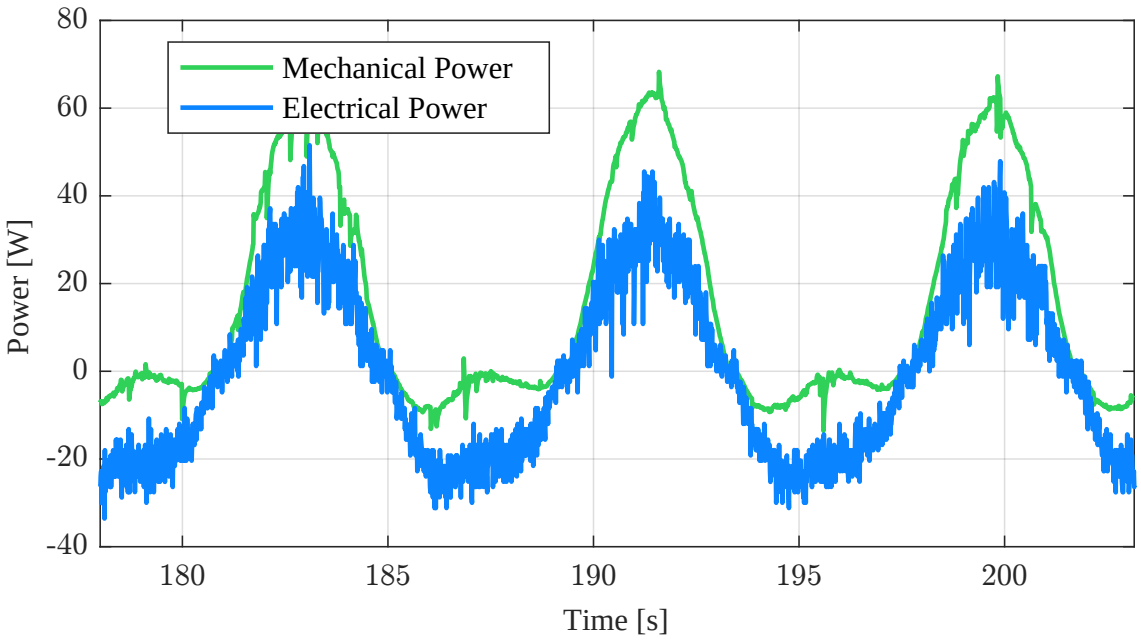

Figure 5.8: Measured mechanical power and electrical power of PTO during three periods.

Figure 5.10 shows the measured power loss and the predicted power loss using the above estimates for armature resistance and damping coefficient.

We can use our estimates to predict the electrical power consumed using the expression we derived in 4.9 and using our measurements of speed and torque. In Figure 5.11 we compare this predicted electrical power to the electrical power we obtain by multiplying measured current and measured voltage.

5.6 Chapter conclusion

In this chapter we described the design and fabrication of two PTO systems. One capable only of reel-in intended for pool testing of a prototype kite, and the other capable of both reel-in and reel-out intended for lake-testing. The second PTO system was designed and fabricated with the ability to integrate an additional

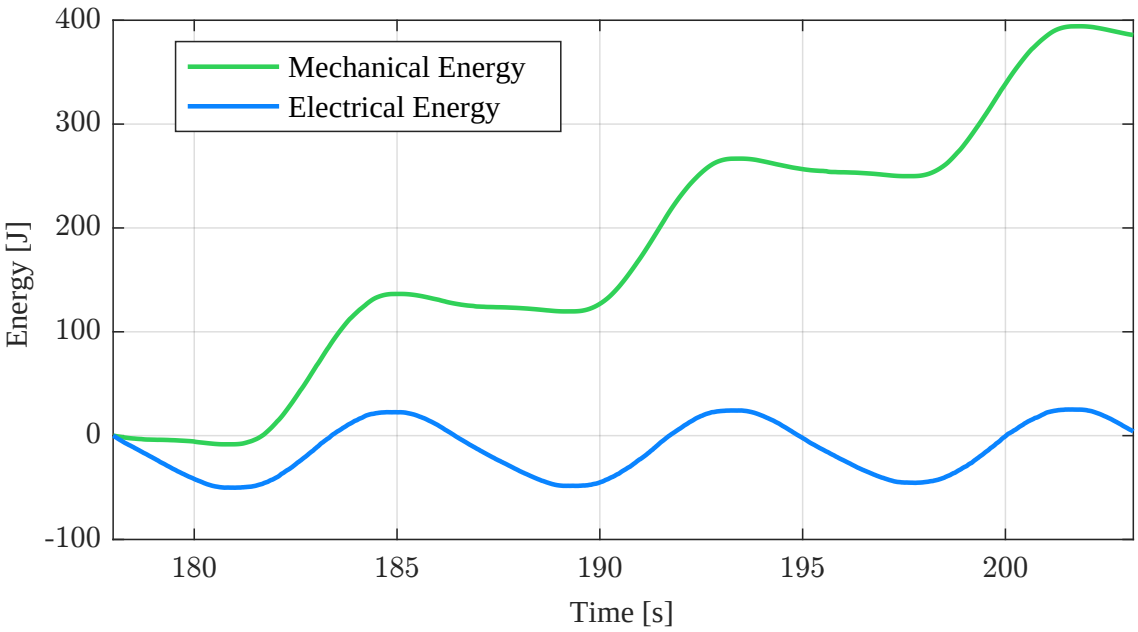

Figure 5.9: Generated mechanical and electrical energy during three periods.

electric motor that was used to evaluate how much electrical power is generated by running open-loop trajectories optimized for mechanical power. We found that the losses in power, that is the difference between mechanical power and reel-in power are significant and greater than what we simulated in the previous chapter. Finally, we used the data from these experiments to estimate the parameters of the electric machine, that is: the armature resistance, the motor constant, and the rotor damping ratio. The identified parameters differed significantly from the assume parameters used in our optimization study in chapter 4 offering a potential explanation to the optimistic results obtained in that chapter. More specifically, the parameters assumed in chapter 4 unrealistically underestimate the losses in the system, and thus also diminish the potential of the optimized trajectories to reduce the power loss to inefficiencies. Future work must include re-optimization of these trajectories using more the more realistic parameters estimated in this chapter.

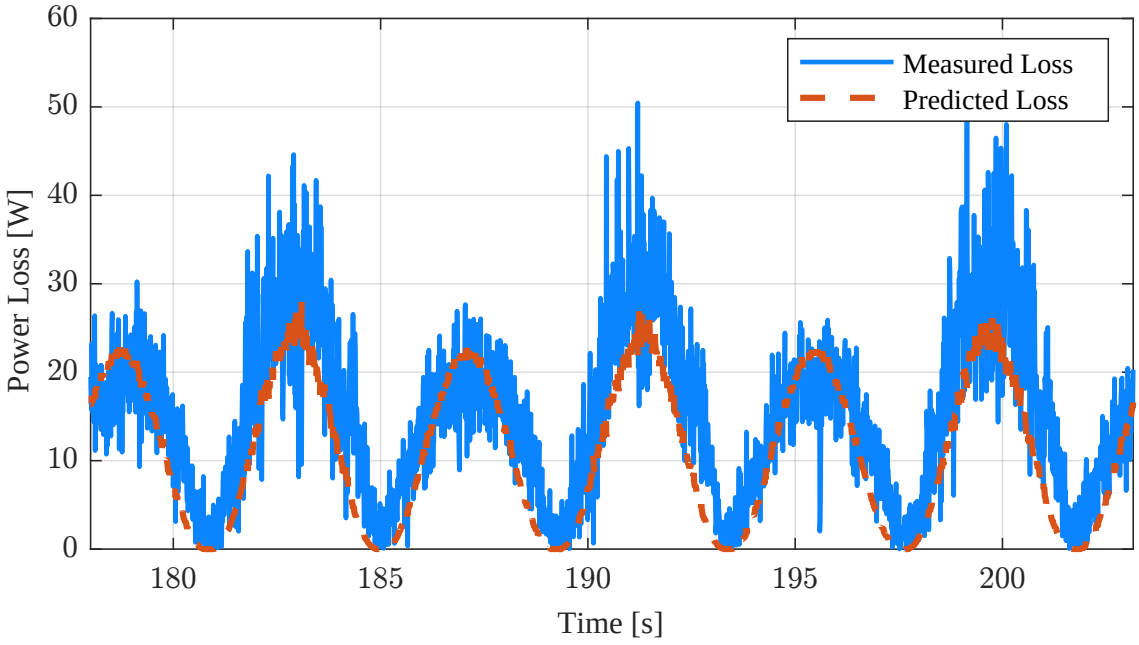

Figure 5.10: Measured power loss and predicted loss using estimated parameters

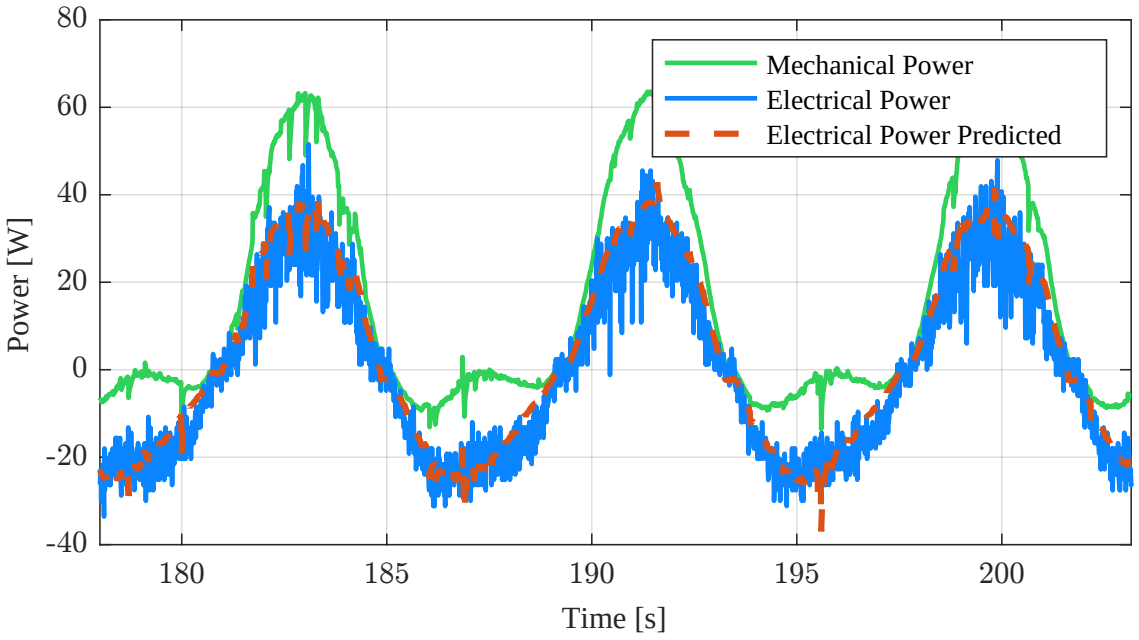

Figure 5.11: Measured mechanical power, measured electrical power, and electrical power prediction w/ estimated parameters

Chapter 6: Summary and Conclusions

6.1 Summary

The goal of this dissertation is to provide the scientific community with model-based algorithms for online optimal trajectory control of a marine hydrokinetic system. We made four research contributions along this overarching goal:

1. An integrated model of the flight and tether dynamics of a marine hydrokinetic energy harvesting system.

2. The trajectory optimization of a marine hydrokinetic kite.

3. The trajectory optimization of a marine hydrokinetic kite accounting for the electrical efficiencies of the power take-off system.

4. The design and fabrication of the power take-off system of a lab-scale marine hydrokinetic energy harverster.

In chapter 2 we derived a simplified 3DOF model and a flexible tether model. For a neutrally buoyant tether with a sufficiently low mass, it is possible to neglect the dynamics of the tether. This allowed us to use this simplified model for optimization. In chapter 3 we used this simplified 3DOF to analytically obtain trajectories

that maximize the mechanical power generated by the system by linearizing our dynamics around a zero-power equilibrium and imposing sinusoidal input trajectories. One important discovery made in this chapter was the degree to which reel-out and reel-in are achieved in the plane perpendicular to the free-stream flow. In chapter 4 we re-formulated our problem to account for the electrical efficiencies. Finally, in chapter 5 we design and fabricated two PTO systems for pool, laboratory, and lake tests. In laboratory tests we evaluated the electric power that is generated by the trajectories optimized for mechanical power. We also used the experimental data to identify the electric parameter of the system.

6.2 Future work

Our parameter identification in chapter 5 yielded results that differ significantly with the empirically obtained parameters used in our optimization work that accounts for the electrical efficiency of the system in chapter 4. Our study suggests that we underestimated the magnitude of the electrical losses in the system, which could explain the small gains obtained by optimizing for accounting these losses. Future work should re-optimize these trajectories using the experimentally identified parameters.

In addition to that, the work presented in chapter 3 assumes the period of the reel-in/reel-out motion is the same as the cross-current motion. Future work should explore the effect of relaxing this restriction makes.

Bibliography

[1] U.S Energy Information Administration. Monthly energy review, September 2020.

[2] Minesto AB. `https://minesto.com/`.

[3] John M. Bane, Ruoying He, Michael Muglia, Caroline F. Lowcher, Yanlin Gong, and Sara M. Haines. Marine hydrokinetic energy from western boundary currents. *Annual Review of Marine Science*, 9(1):105–123, jan 2017.

[4] Chris Vermillion and Lorenzo Fagiano. Electricity in the air: Tethered wind energy systems. *Mechanical Engineering*, 135(09):S13–S21, 2013.

[5] Miles L. Loyd. Crosswind kite power (for large-scale wind power production). *Journal of Energy*, 4(3):106–111, may 1980.

[6] Antonello Cherubini, Rocco Vertechy, and Marco Fontana. Simplified model of offshore Airborne Wind Energy Converters. *Renewable Energy*, 88:465–473, April 2016.

[7] Ja Alvarez-Gallegos, Rafael Castro-Linares, and MA Zempoalteca-Jimenez. Robust nonlinear flight control of a power-generating tethered kite. In *2019 16th International Conference on Electrical Engineering, Computing Science and Automatic Control (CCE)*, pages 1–6. IEEE, 2019.

[8] Michael Erhard and Hans Strauch. Flight control of tethered kites in autonomous pumping cycles for airborne wind energy. *Control Engineering Practice*, 40:13–26, July 2015.

[9] Ali Baheri and Chris Vermillion. Waypoint optimization using bayesian optimization: A case study in airborne wind energy systems. In *2020 American Control Conference (ACC)*, pages 5102–5017. IEEE, 2020.

[10] Uwe Fechner, Rolf van der Vlugt, Edwin Schreuder, and Roland Schmehl. Dynamic model of a pumping kite power system. *Renewable Energy*, 83:705–716, 2015.

[11] M. Kehs, C. Vermillion, and H. Fathy. Online energy maximization of an airborne wind energy turbine in simulated periodic flight. *IEEE Transactions on Control Systems Technology*, 26(2):393–403, 2018.

[12] Jonas Koenemann, Paul Williams, Soeren Sieberling, and Moritz Diehl. Modeling of an airborne wind energy system with a flexible tether model for the optimization of landing trajectories. volume 50, pages 11944–11950. Elsevier, jul 2017.

[13] L. Fagiano, A. U. Zgraggen, M. Morari, and M. Khammash. Automatic Crosswind Flight of Tethered Wings for Airborne Wind Energy: Modeling, Control Design, and Experimental Results. *IEEE Transactions on Control Systems Technology*, 22(4):1433–1447, July 2014.

[14] Sean Costello, Grégory François, and Dominique Bonvin. Crosswind kite control–a benchmark problem for advanced control and dynamic optimization. *European Journal of Control*, 35:1–10, may 2017.

[15] Chris Vermillion. Altitude and crosswind motion control for optimal power-point tracking in tethered wind energy systems with airborne power generation. In *Dynamic Systems and Control Conference*, volume 56147, page V003T49A001. American Society of Mechanical Engineers, 2013.

[16] H. Li, D. J. Olinger, and M. A. Demetriou. Control of a tethered undersea kite energy system using a six degree of freedom model. In *2015 54th IEEE Conference on Decision and Control (CDC)*, pages 688–693, 2015.

[17] H. Li, D. J. Olinger, and M. A. Demetriou. Passivity based control of a tethered undersea kite energy system. In *2016 American Control Conference (ACC)*, pages 4984–4989, 2016.

[18] Zhe Liu, Yi Zhao, Yuerong Zhou, and Faming Guan. Modeling, simulation and test results analysis of tethered undersea kite based on bead model. *Renewable Energy*, 154:1314–1326, jul 2020.

[19] Shubham Tandon, Sathvik Divi, Michael Muglia, Christopher Vermillion, and Andre Mazzoleni. Modeling and dynamic analysis of a mobile underwater turbine system for harvesting Marine Hydrokinetic Energy. *Ocean Engineering*, 187:106069, September 2019.

[20] Ayaz Siddiqui, Kartik Naik, Mitchell Cobb, Kenneth Granlund, and Chris Vermillion. Lab-scale, closed-loop experimental characterization, model refinement, and validation of a hydrokinetic energy-harvesting ocean kite, aug 2020.

[21] Paul Williams, Peter Lapthorne, and Pavel Trivailo. Circularly-towed lumped mass cable model validation from experimental data. In *AIAA Modeling and Simulation Technologies Conference and Exhibit*. American Institute of Aeronautics and Astronautics, aug 2006.

[22] Paul Williams, Bas Lansdorp, and Wuboo Ockels. Modeling and control of a kite on a variable length flexible inelastic tether. In *AIAA Modeling and Simulation Technologies Conference and Exhibit*. American Institute of Aeronautics and Astronautics, aug 2007.

[23] F. R. Driscoll, R. G. Lueck, and M. Nahon. Development and validation of a lumped-mass dynamics model of a deep-sea rov system. *Applied Ocean Research*, 22(3):169–182, jun 2000.

[24] C. M. Ablow and S. Schechter. Numerical simulation of undersea cable dynamics. *Ocean Engineering*, 10(6):443–457, jan 1983.

[25] Aldo U Zgraggen, Lorenzo Fagiano, and Manfred Morari. On real-time optimization of airborne wind energy generators. In *52nd IEEE Conference on Decision and Control*, pages 385–390. IEEE, 2013.

[26] A. U. Zgraggen, L. Fagiano, and M. Morari. Real-time optimization and adaptation of the crosswind flight of tethered wings for airborne wind energy. *IEEE Transactions on Control Systems Technology*, 23(2):434–448, 2015.

[27] Michael Erhard, Greg Horn, and Moritz Diehl. A quaternion-based model for optimal control of an airborne wind energy system. *ZAMM - Journal of Applied Mathematics and Mechanics / Zeitschrift für Angewandte Mathematik und Mechanik*, 97(1):7–24, 2017.

[28] Jeroen Stuyts, Greg Horn, Wouter Vandermeulen, Johan Driesen, and Moritz Diehl. Effect of the electrical energy conversion on optimal cycles for pumping airborne wind energy. *IEEE Transactions on Sustainable Energy*, 6(1):2–10, jan 2015.

[29] J. Deese and C. Vermillion. Recursive Gaussian Process-Based Adaptive Control, With Application to a Lighter-Than-Air Wind Energy System. *IEEE Transactions on Control Systems Technology*, pages 1–8, 2020.

[30] Mitchell Cobb, Kira Barton, Hosam Fathy, and Chris Vermillion. An iterative learning approach for online flight path optimization for tethered energy systems undergoing cyclic spooling motion. pages 2164–2170. IEEE, 2019.

[31] M. K. Cobb, K. Barton, H. Fathy, and C. Vermillion. Iterative learning-based path optimization for repetitive path planning, with application to 3-d crosswind flight of airborne wind energy systems. *IEEE Transactions on Control Systems Technology*, 28(4):1447–1459, 2020.

[32] G. Mademlis, Y. Liu, P. Chen, and E. Singhroy. Design of maximum power point tracking for dynamic power response of tidal undersea kite systems. *IEEE Transactions on Industry Applications*, 56(2):2048–2060, 2020.

[33] Miguel Alvarez, Debapriya Bhattacharjee, Chris Vermillion, and Hosam K. Fathy. An integrated model of the flight and tether dynamics of a marine hydrokinetic energy harvesting system. In *2021 European Control Conference (ECC) . IEEE*, 2021.

[34] Miguel Alvarez and Hosam K. Fathy. Outcomes and insights from simplified analytic trajectory optimization for a tethered underwater kite. *IEEE L-CSS*, September 2021. [In Review].

[35] Moritz Diehl. Airborne wind energy: Basic concepts and physical foundations, 2013.

[36] Pragasen Pillay and Ramu Krishnan. Modeling, simulation, and analysis of permanent-magnet motor drives. ii. the brushless dc motor drive. *IEEE transactions on Industry applications*, 25(2):274–279, 1989.